Title:
**Probabilistic assimilation of optical satellite data with physiologically based growth functions improves crop trait time series reconstruction**

Authors:

Lukas Valentin Graf, ETH Zürich (lukasvalentin.graf@usys.ethz.ch)
Flavian Tschurr, ETH Zürich (flavian.tschurr@usys.ethz.ch)
Achim Walter, ETH Zürich (achim.walter@usys.ethz.ch)
Helge Aasen, Agroscope (helge.aasen@agroscope.admin.ch)

Corresponding author: Lukas Valentin Graf

# Highlights

**Probabilistic assimilation of optical satellite data with physiologically based growth functions improves crop trait time series reconstruction**

Lukas Valentin Graf, Flavian Tschurr, Achim Walter, Helge Aasen

- Physiological knowledge improved crop trait time series reconstruction
- Physiological based growth functions are assimilated with optical satellite data
- A probabilistic data assimilation scheme accounts for uncertainties
- Bias in remotely sensed Green Leaf Area time series is reduced
- The results were validated at multiple sites

# Probabilistic assimilation of optical satellite data with physiologically based growth functions improves crop trait time series reconstruction

Lukas Valentin Graf[a,b,*], Flavian Tschurr[a], Achim Walter[a], Helge Aasen[a,b]

[a] *Crop Science, Institute of Agricultural Science, ETH Zurich, Universitaetstrasse 2, 8092 Zurich, Switzerland*

[b] *Earth Observation of Agroecosystems Team, Division Agroecology and Environment, Agroscope, Reckenholzstrasse 191, 8046 Zurich, Switzerland*

## Abstract

A sound understanding of plant growth is critical to maintaining future crop productivity under ongoing climate change. Remotely sensed time series of crop functional traits from optical satellite imagery are an invaluable tool for deriving appropriate management practices that facilitate risk mitigation and increase the resilience of agroecosystems. However, the availability of imagery is limited by atmospheric disturbances that cause large temporal gaps and noise in the trait time series. Therefore, time series reconstruction methods are required for accurate crop growth modelling. Physiological priors, such as the fact that plant growth is mainly controlled by a few environmental covariates, among which air temperature plays a prominent role, represent a promising approach to improve the representation of crop growth. Here, a novel approach is proposed that combines Sentinel-2 Green Leaf Area Index (GLAI) observations with three dose response curve approaches describing the a priori physiological relationship between growth and temperature in winter wheat. A probabilistic ensemble Kalman filtering data assimilation scheme allows the com-

* *Email address:* lukasvalentin.graf@usys.ethz.ch (Helge Aasen)

*Preprint submitted to ISPRS Journal of Photogrammetry and Remote Sensing November 13, 2023*

bination of high temporal resolution air temperature data and satellite imagery, which also allows quantification of uncertainties. The proposed approach requires a smaller number of satellite observations compared to conventional remote sensing time series algorithms, making it suitable for agricultural areas with high cloud cover, and is considerably less complex than a mechanistic crop growth model. Validation was carried out using in-situ data collected on winter wheat plots in Switzerland in two consecutive years. The validation results suggest that the proposed assimilation of Sentinel-2 GLAI and temperature-response-based growth rates allows the reconstruction of physiologically meaningful GLAI time series. In particular, the systematic underestimation of high in-situ GLAI values ($> 5\ m^2\ m^{-2}$) often prevalent in purely remote sensing driven GLAI time series reconstruction was reduced. Thus, the proposed approach is advantageous compared to state-of-the-art remote sensing approach based on wide-spread logistic functions by means of physiological plausibility, fitting requirements and representation of high in-situ GLAI values. This has great potential to increase the reliability of remotely sensed crop productivity assessment.

*Keywords:* Green Leaf Area Index, Sentinel-2, Physiology, Time Series, Crop Growth Modeling, Crop Productivity

## 1. Introduction

The majority of daily calorie intake is provided by a few arable crops, including wheat. Ongoing climate change poses a major challenge to the ability of such crops to produce resilient yields (Asseng et al., 2015). This calls for suited management practices to mitigate risks and increase the resilience of agroecosystem. Consequently,

a sound understanding of plant growth is urgently needed to identify and minimise crop risks (Tilman et al., 2011). Plant growth dynamics within different phenological phases can be of great interest to identify stressors (Reynolds and Langridge, 2016). An important phase with respect to the yield potential of winter wheat (*Triticum aestivum*) is the stem elongation phase (i.e., begin of stem elongation until begin of flowering), which will be the focus of this study (Kronenberg et al., 2017; Miralles et al., 2000).

Using optical satellite remote sensing, plant growth can be recorded on large spatial scales with relatively high temporal resolution. Remotely sensed time series of functional crop traits such as green leaf area index (GLAI) – defined as the photosynthetically active leaf area per unit ground area (Maddonni and Otegui, 1996) – are therefore widely used to estimate vegetation productivity (Kooistra et al., 2023). For time series reconstruction, mainly statistical models are used, which fit a function to a set of satellite observations. Over the past decades, a variety of these statistical reconstruction models have been proposed (Zeng et al., 2020; Kooistra et al., 2023). These models range from simple linear interpolation to models that already incorporate prior knowledge about vegetation development, such as double logistic models (DL) (Beck et al., 2006). DL take advantage of the fact that most crop traits follow a bell curve with an ascending branch for the generative phase and a descending branch for the senescent phase. DL are therefore a clear advancement compared to time series reconstruction methods such as the Savitzky-Golay filter (Savitzky and Golay, 1964), the Whittaker smoother (Eilers, 2003), or Gaussian processes regression (Belda et al., 2020; Pipia et al., 2021) that lack a explicit

formulation of basic principles of crop growth and development. DL can be used to plausibilize the estimation of functional crop traits, i.e., to check whether temporal trajectories are consistent with prior knowledge (Koetz et al., 2005). Strictly speaking, this reconstruction is a modeling of crop growth.

Still, even such advanced models depend on the availability of a sufficiently high number of satellite observations. The number of observations in optical remote sensing, however, can be reduced significantly by unfavorable atmospheric conditions such as clouds. In mid-latitude environments, which represent a major part of the world's wheat production area, the percentage of cloudy optical satellite images can be higher than 60% (Sudmanns et al., 2020). This leads to larger temporal gaps in the data which constrain time reconstruction accuracy (Zhou et al., 2015). Moreover, undetected clouds and shadows, i.e., noise, can deteriorate the quality of time series reconstruction (Zhou et al., 2016). This is significant as the reconstruction methods approach crop growth modeling mainly from a statistical perspective, i.e., they make strong assumptions about the distribution and power of signal and noise. Moreover, the model parameters of statistical methods such as the aforementioned Whittaker smoother or Savitzky-Golay filter have often no intrinsic biological or physical meaning. Thus, the physiological plausibility of the reconstructed time series is not guaranteed resulting in a potentially misleading representation of crop growth. Nevertheless, the acceptance of these models in the remote sensing community is high (Kooistra et al., 2023) as the models are usually fast and easy to use.

A more advanced perspective on crop growth and development is provided by

mechanistic crop models that address the underlying physiological processes (Delécolle et al., 1992; Jamieson et al., 1998; Keating et al., 2003). Mechanistic, or process based, models are explicit formulations of physical and biological processes, with physical and biological meaning assigned to all parameters of the model (Cox et al., 2006). However, these models require extensive calibration efforts and information about boundary conditions such as soil properties which are often not available. To address this issue, the assimilation of remotely sensed functional traits has been proposed (Pellenq and Boulet, 2004) and shown to improve vegetation productivity estimation (Huang et al., 2019; Waldner et al., 2019). Still, the complexity of mechanistic models and lack of calibration data limit their use in agricultural remote sensing (Weiss et al., 2020) although more simpler models such as the simple algorithm for yield estimation (SAFYE) have been proposed (Ma et al., 2022).

From a purely physiological perspective, temperature is one of the most important and yet easy to measure covariates controlling plant growth (Porter and Gawith, 1999; Asseng et al., 2019). A simple and widely used example in this regard is the concept of growing degree days (GDD) (Mcmaster, 1997). GDD describe the change of a trait value, i.e., growth, as the accumulation of temperature sums. This, however, partly neglects the effect that any chemical and, hence, biological process takes place within a specific temperature range and that reaction (growth) rates are a function of temperature. In detail, there is a minimum or base temperature $T_{base}$ below which no growth occurs as well as a maximum temperature $T_{max}$ above which growth comes to a halt. Between $T_{base}$ and $T_{max}$ there is an optimal temperature, $T_{opt}$, at which the growth rate reaches its maximum (Porter and Gawith, 1999).

Various dose response curve (DRC)s have been proposed to model growth as a function of temperature (Wang et al., 2017). The range of functions varies from the above GDDs to the use of more complex functions such as asymptotic curves (Roth et al., 2022), the curve proposed by Wang and Engel (1998) or the Arrhenius-shaped curve proposed in Parent and Tardieu (2012). The parameters of the DRCs have – like mechanistic crop models – a biological meaning, but require only a few parameters, which arguably makes them easy to use. Roth et al. (2022) have shown that crop growth rates under field conditions can be accurately reconstructed from DRCs. The authors have also shown that DRCs based on hourly air temperature data allow interpolation of coarser resolution (every three to four days) trait observations. However, to the best of our knowledge, a DRC-based time series reconstruction approach has not been used to interpolate between satellite-derived crop trait observations.

Our primary objective is therefore to use a priori physiological knowledge of the dependence of plant growth on air temperature encoded in DRCs to improve the reconstruction of GLAI time series from a set of satellite observations. We hypothesise that the use of physiologically informed DRCs and high spatial resolution trait observations will provide an accurate, physiologically consistent representation of crop growth. We therefore assume DRCs to outperform statistical time series reconstruction methods that lack an explicit linkage to biology.

Based on our objective, we formulate three research questions:

- First, can DRC crop growth rates be used to reconstruct continuous, physiologically plausible crop trait time series from a set of satellite observations?
- Second, does the proposed approach outperform a time series reconstruction

based on remote sensing data alone in terms of accuracy and reliability?

- Third, what temporal resolution of temperature data is required - hourly or daily?

To address these questions, we focus on GLAI derived from the Sentinel-2 (S2) satellite constellation at a study region in Switzerland, which acts as a blue-print for intensively farmed agricultural landscapes in temperate climate zones.

We start with a description of the in-situ GLAI data used to calibrate and validate our proposed methodology (Section 2). We then describe the fitting of the DRCs to encode a-priori physiological knowledge. We continue with the GLAI retrieval from S2 to introduce spatial detail and large area coverage, and the proposed probabilistic reconstruction scheme in Section 3 alongside a baseline method based on S2 GLAI observations, only.

## 2. Data

### *2.1. Data*

#### *2.1.1. Calibration Data*

Three sites in Switzerland (CH Bramenwies), western (Rur catchment, DE-Rur) and south-eastern Germany (Munich-North-Isar, DE-MNI) were used for calibration, i.e., for establishing the physiological a-priori knowledge. The data cover several winter wheat growing seasons. The sites represent winter wheat field parcels operated by farmers according to local agricultural management practice (see Table 1 for an overview).

At all sites, GLAI measurements (section 3.1.2) and phenology (section 3.1.3) ratings were carried out, which were linked to hourly air temperature from nearby weather stations. The GLAI measurements were chosen to represent the generative phase of the growing season, within which the GLAI should increase over time, i.e., the beginning of stem elongation to heading. In total the calibration data set contains 890 data points with the corresponding temperature history (Table 1). The dataset contains a total of 11 environments (year × location), providing a representative data set for model calibration in temperate environments of central Europe. Further details about the sites are provided in the following paragraphs.

Table 1: Calibration data with locations, years, the corresponding amount of GLAI measurements, and reference of the dataset. Latitude and longitude are provided in geographic coordinates (WGS-84).

| Location | Years | GLAI measurements | Lat. | Lon. | Reference |
|---|---|---|---|---|---|
| CH Bramenwies | 2022 | 840 | 47.45 | 8.69 | Wildhaber et al. (2023) |
| DE MNI | 2017, 2018, 2020, 2021, 2022 | 24 | 48.29 | 11.71 | Danner et al. (2017), Danner et al. (2019), Wocher et al. (2018) |
| DE Rur | 2008, 2009, 2010, 2013, 2015 | 26 | 50.87 | 6.44 | Reichenau et al. (2020) |

*CH Bramenwies.* At the Bramenwies site in northern Switzerland (47.45° N, 8.69° E, 550 m above sea level), 840 GLAI were measured within a single winter wheat

field parcel (2.04 ha) at 29 predefined sampling points during the growing season of 2022. The area receives a total annual precipitation of 1200 mm and has an annual air temperature of 10 °C (reference period 2011 to 2022). The soil of the moderately sloping parcel is loamy (clay content 20 to 30%) and slightly alkaline (pH between 7.2 and 7.8) with moderate humus content (3.0 to 3.6%). The parcel was managed according to Swiss standards for conventional agriculture with three applications of mineral fertiliser in April and May 2022 (Wildhaber et al., 2023). Meteorological data were available from a weather station operated by the Agrometeorological Network of the Institute for Excellence in Agricultural Research, Agroscope.

*DE MNI.* 24 GLAI measurements in winter wheat from five years between 2017 and 2022 were available at the MNI site (48.29° N, 11.71° E, 440 m above sea level) close to the river Isar ($\leq$ 10 km) north of the city of Munich. Measurements were taken between the beginning of April and July each year. The average annual air temperature is about 8.9 degrees Celsius with an annual precipitation of 757 mm (reference period 1991 to 2020). The dominant soil types in the mostly flat area are gleysols and pararendzina of alluvial origin. The parcels were managed according to conventional agricultural practices following German standards (Danner et al., 2017, 2019; Wocher et al., 2018). Weather data was obtained from a station operated by the German Meteorological Service at Munich Airport.

*DE Rur.* At the Rur catchment in northwestern Germany, 26 GLAI measurements were made in five years between 2008 and 2015 (50.87° N, 6.44° E, 100 m above sea level) in a fertile loess plain characterised by luvisols and anthrosols (Reichenau et al., 2020). From the original dataset of Reichenau et al. (2020) we took GLAI

observations in winter wheat from the sites Merzenhausen, Selhausen and Merken. The mean annual air temperature at these sites is about 10 degrees C and the total annual precipitation is about 700 mm. The fields were managed conventionally according to local best agricultural practice. Weather data were measured at stations located close to the monitored plots.

### *2.2. Validation Data*

Independent data to validate the reconstructed GLAI time series were collected in 2022 and 2023 on seven winter wheat parcels at the Strickhof and Swiss Future Farm sites in northern Switzerland. The location of the sites and the shapes of the field plots are shown in Figure 1a. A sampling design of between three and eight sampling points per parcel was chosen to capture the heterogeneity within fields (white dots in Figure 1a). All sites are located in the Swiss Central Plateau, which is characterised by a temperate climate (mean annual air temperature around 10°C) and humid conditions (annual precipitation around 1000 mm). Both sites are equipped with weather stations operated by the Swiss Federal Office of Meteorology and Climatology, MeteoSwiss (Swiss Future Farm) and the AgroMeteo network of the Swiss Federal Centre of Excellence for Agricultural Research, Agroscope (Strickhof), which provide hourly air temperature measurements.

The fields were managed according to Swiss conventional agricultural practice. Detailed management information including the sowing date, winter wheat variety as well as timing and amount of fertilizer applied was provided by the farmers.

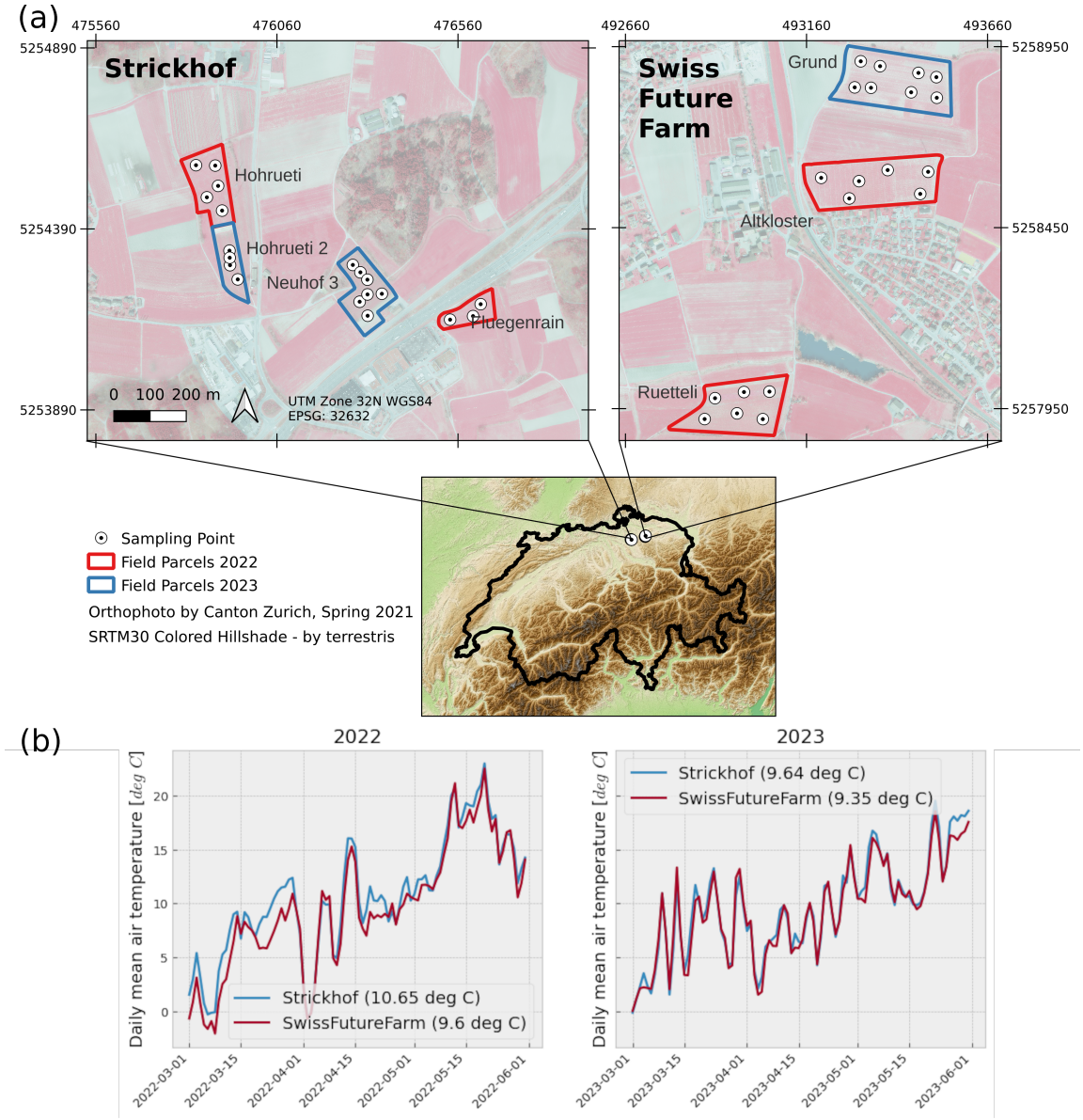


Figure 1: (a) Map of the two sites at which independent validation data was acquired in 2022 (red) and 2023 (blue). Dots denote the position of the sampling points in the field parcels to capture field heterogeneity. (b) Daily mean air temperature 2 m above ground at the validation sites in spring 2022 (left) and 2023 (right). The mean air temperature between 1st of March and 30th of June is given in the legend in brackets.

194 In terms of meteorology, 2022 and 2023 were different: 2022 had a dry and

warm spring, while April and May of 2023 were rainy and higher temperatures only occurred towards the end of May. Figure 1b shows the daily mean air temperatures for the Strickhof (blue) and Swiss Future Farm (red) sites in 2022 (left) and 2023 (right). In both years the Strickhof site was warmer than the Swiss Future Farm site. In 2022, the mean air temperature between the beginning of March and June was 10.65 and 9.6 degrees C for Strickhof and Swiss Future Farm, respectively. In 2023 this value decreased to 9.64 and 9.35 degrees C respectively.

### *2.3. Sentinel-2 Imagery*

Thanks to its twin-constellation of S2A and B, the S2 platform provides high revisit rates (<= 5 days in mid-latitudes) and captures spectral reflectance data in 13 channels between 490 and 2200 nm in up to 10 m spatial resolution. S2 has therefore proven an invaluable data source for vegetation studies including the retrieval of crop functional traits (Amin et al., 2021; Delloye et al., 2018, for instance).

We obtained S2 bottom-of-atmosphere (processing level: L2A) imagery from Microsoft Planetary Computer[1] using the open-source Python library EOdal (Graf et al., 2022) (version 0.2.1; Python 3.10). The data cover the validation sites (Figure 1). We used all scenes in 2022 and 2023 between the beginning and ending of the stem elongation phase (i.e., April to June) with a scene-wide cloud cover threshold of $\leq$ 50%. We determined the date range considered per parcel from the in-situ ratings of phenology (Section 3.1.3). In addition, we used a scene before and after the determined time period to provide enhanced temporal context and account for

[1] `https://planetarycomputer.microsoft.com/`

uncertainty regarding the exact onset of the phenological development stages. In total, 17 S2 scenes were available at the Strickhof site in 2022 and 14 in 2023, while at the Swiss Future Farm site 14 and 11 scenes could be used in 2022 and 2023, respectively.

## 3. Methods

Figure 2 shows the proposed workflow. Based on in-situ GLAI (*"in-situ GLAI"*) values and air temperature data at the calibration sites (Section 2.1.1), DRCs are fitted and used to model growth rates in hourly and daily resolution (Figure 2a). S2 GLAI (*"raw GLAI"*) observations at the validation sites (Section 2.2, Figure 2b) are assimilated into the DRC-based growth curves and used to reconstruct the GLAI time series (*"DRC GLAI"*) (Figure 2c). In addition, a baseline is fit based solely on S2 GLAI observations (*"baseline GLAI"*) using a sigmoid function (Figure 2d). In a last step, the reconstructed GLAI time series are compared to in-situ validation data. The term "coarse spatial resolution", as depicted in Figure 2, indicates that the meteorological data offered only one reading for each field parcel, without accounting for any within-field variability. On the other hand, high spatial resolution implies that the spatial intricacies regarding within-field heterogeneity are taken into account. Code and data necessary to reproduce all processing and analysis are available under GNU General Public License v3.0[2]. The methods section follows this structure and starts with the processing of the in-situ data.

[2] `https://github.com/EOA-team/sentinel2_crop_trait_timeseries`

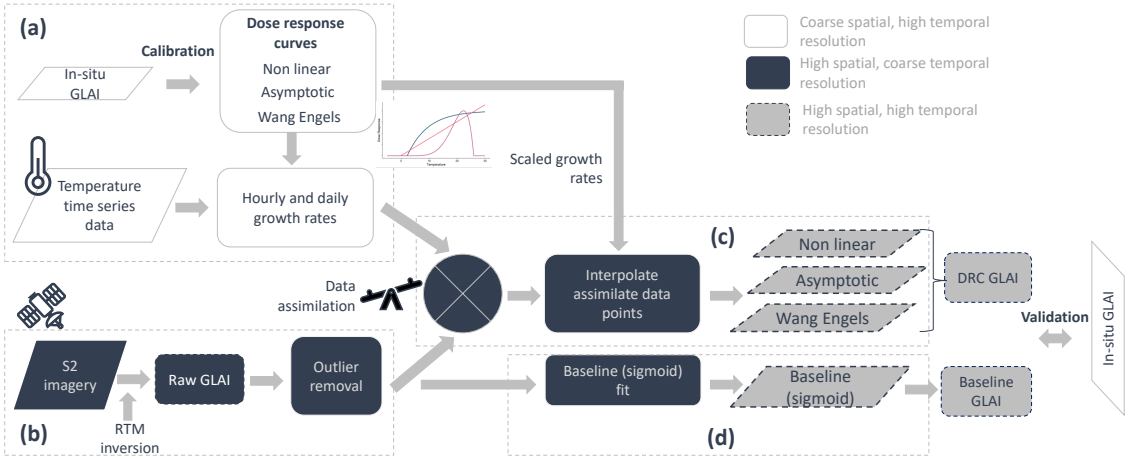


Abbreviations: DRC – Dose response curve; GLAI – Green leaf area index; RTM – Radiative transfer model; S2 – Sentinel-2

Figure 2: Proposed workflow to reconstruct continuous GLAI time series with high spatial and temporal resolution using temperature-based DRCs to obtain GLAI growth rates (a), S2 raw GLAI observations per pixel (b) and data assimilation and DRC-based interpolation of assimilated DRC GLAI values (c). The baseline method using a sigmoid function fit to the S2 GLAI data (baseline GLAI) is shown in (d).

### *3.1. Processing of in-situ data*

Throughout the main growing season of winter wheat (beginning of March till end of June in central Europe) continuous, mostly weekly measurements of GLAI and phenology were undertaken at the calibration (Section 2.1.1) and validation sites (Section 2.2). All measurements were linked to hourly air temperature readings 2 m above ground available from nearby weather stations.

#### *3.1.1. Air temperature data*

Air temperature data was acquired hourly 2 m above ground in deg C. In addition, the temperature readings were aggregated to daily resolution by averaging all 24 hourly measurements of a day from midnight to midnight.

### *3.1.2. Green Leaf Area Index*

GLAI samples were derived non-destructively using a LAI-2200C Plant Canopy Analyzer by LI-COR Biosciences with a 45 degree viewing cap. Measurements were performed at pre-defined sampling points within the fields (see, e.g., Figure 1a). For each measurement, three replicates were performed in different orientations each of them offset by 90 degrees. To avoid contamination of the measurement by direct sun light the measurements were either shaded manually, taken under diffuse light conditions (over-cast sky, fog) or acquired early in the morning.

### *3.1.3. Phenology*

Estimates of GLAI (Section 3.1.2) were linked to phenological development. Phenological development of the winter wheat canopies was expressed in Biologische Bundesanstalt, Bundessortenamt and CHemical Industry (BBCH) scale following Lancashire et al. (1991). For the rating of the beginning of stem elongation (BBCH 30) we cut the main tiller lengthwise and measured the distance between the first node and the tillering node following the manual by Pask et al. (2012). End of heading (BBCH 59) was reached when the inflorescence was fully emerged.

## *3.2. Model calibration to introduce physiological knowledge*

Model calibration introduces the a-priori physiological knowledge about the relationship between plant growth and air temperature (Figure 2a). The knowledge was based on a dataset of in-situ GLAI measurements from the calibration sites (Section 2.1.1). The measured in-situ GLAI values were used to calculate $\Delta$ green leaf area index ($\Delta$GLAI) between two time points, which represent increase, respectively

growth of the wheat canopy (Equation 1) (as in Tschurr et al. (2023)). In-situ GLAI values have been smoothed using cubic smoothing splines before the calculation of ΔGLAI.

$$\Delta GLAI(t_n) = GLAI(t_n) - GLAI(t_{n-1})\,, \tag{1}$$

The ΔGLAI value can then be expressed using the temperature trajectory between time point $t_n$ and $t_{n-1}$ in either hourly or daily granularity.

### *3.2.1. Fitting of Dose-Response Curves*

The calibration dataset was utilised to optimise three distinct DRC, as illustrated in Figure 3. Each curve represents the behaviour of the ΔGLAI as a function of the observed temperature. The simplest DRC displays a non-linear correlation between growth and temperature, with zero growth deemed below $T_{base}$. A linear growth reaction is projected for temperatures exceeding $T_{base}$. We hereafter refer to this growth response curve as the non-linear DRC (e.g., as seen in Roth et al. (2023)). Additionally, an asymptotically shaped DRC was employed, accounting for a base temperature ($T_{base}$), below which no growth occurs. Above $T_{base}$, the DRC exhibits a maximum growth response, defined by the curve's asymptote, along with the parameter lrc, allowing for an asymptotic shape of the curve (e.g., see Roth et al. (2022)). Similar to the asymptotic DRC, the Wang Engels DRC can be defined by three parameters: $T_{base}$, which is the temperature below which growth does not occur, $T_{opt}$, which defines the highest growth rate response, and $T_{max}$, which is the temperature above which the growth rate is set to zero (Wang and Engel, 1998; Wang et al., 2017)

288 (refer to Figure 3).

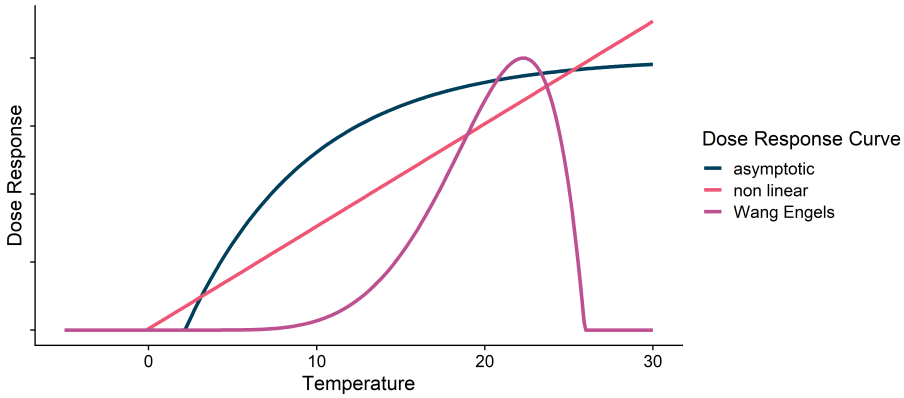


Figure 3: Schematic overview of the three used dose response curves (DRC), non linear, asymptotic and Wang Engels curve. The x axis represents the input temperature, the y axis the corresponding response in green leaf area index (GLAI) growth.

Table 2: Dose response curve parameters and constraints used for model fitting.

| Dose response curve | parameters | constraints |
|---|---|---|
| non linear | $T_{base}$ , slope | |
| asymptotic | $T_{base}$, lrc, asymptote | $T_{base}$ <asymptote |
| | $T_{base}$, | $T_{base}$ |
| Wang Engels | $T_{opt}$, | $<T_{opt}$ |
| | $T_{max}$ | $<T_{max}$ |

289 The parameters for each of the three DRCs (refer to Table 2) were optimised
290 utilising the calibration data explained earlier. An augmented Lagrangian algorithm
291 employing the nloptr package in R (R Core Team, 2018; Johnson, 2007) was used
292 for this purpose. Regarding our third research question, optimisation was conducted
293 for temperature values of both hourly and daily measurements.

As the curves used can solely depict ascending GLAI values, we excluded negative $\Delta$GLAI values prior to optimization. These values are typically attributable to measurement uncertainty and imprecisions, such as those related to sensor positioning. As a result, 20% of $\Delta$GLAI values were rejected. Constrained optimization by linear approximation (COBYLA) was used as the local solver for optimization, providing upper and lower bounds and a starting value (Powell, 1994). Initial values were determined either by quantile values of input temperature data (for $T_{base}$, $T_{opt}$, and $T_{max}$) or by empirically derived values (slope, lrc, and asymptote) (refer to Table A.7 in the Appendix A). Optimisation was carried out 20 times on a randomly selected 80% of the data, and the final parameters were derived from the median of the 20 subset optimisations to obtain more robust parameter values, thereby reducing the possible influence of outliers. For each temperature measurement, the corresponding dose response value was calculated and accumulated over time. To optimise the parameters, the root mean squared error (RMSE) between these accumulated values and the $\Delta$GLAI measurements was minimised. The skill score was negatively impacted for meeting constraints (Table 2) or for forecasting $\Delta$GLAI values that were too low to attain physiologically significant parameter and prediction values.

### *3.3. Processing of S2 data*

S2 raw GLAI observations introduce spatial detail (Figure 2b). We used all 10 and 20 m bands except band 8 (central wavelength 842 nm). Band 8 was discarded in favor of band 8A (central wavelength 865 nm) which provides a higher spectral resolution than band 8. Thus, nine bands between 492 and 2200 nm were used: B2 (blue), B3 (green), B4 (red), B5 (red-edge 1), B6 (red-edge 2), B7 (red-edge 3), B8A

(near-infrared 2), B11 (shortwave-infrared 1), and B12 (shortwave-infrared 2). See also Table A.6 in the Appendix A for details about the native spatial resolution, spectral band widths and central wavelengths of these bands.

First, we clipped the S2 data to the spatial extent of the field parcels at the validation sites (Figure 1a). Next, we resampled the six 20 m bands (see Table A.6) to a spatial resolution of 10 m using nearest neighbor interpolation.

All scenes were pre-processed by ESA using the payload data ground segment (PDGS) baselines 4.00 (2022 data) and 5.09 (2023 data) that compromise an improvement radiometric harmonization of S2A and S2B as well as geometric refinements that fulfil the CEOS Analysis Ready Data for Land (CEOS ARD) standard. Therefore, no further refinements such as image co-registration were undertaken.

### *3.3.1. Data cleaning*

We used the scene classification layer (SCL) delivered as part of the S2 L2A product to filter out clouds, shadows, open water, snow and cirrus on a per-pixel basis. Thus, only the SCL classes 4 (vegetation) and 5 (bare soil) were kept. Pixel values with a different SCL class assignment were masked and not considered any further.

### *3.3.2. Radiative transfer modelling*

To extract raw GLAI from S2 scenes at the validation sites (Section 2.3) we used the four-stream radiative transfer model (RTM) PROSAIL (Jacquemoud et al., 2009) to simulate bi-directional reflectance factors of winter wheat canopies. PROSAIL couples the leaf RTM PROSPECT-D (Féret et al., 2017) with the canopy RTM

4SAIL (Verhoef, 1984). We parameterized the RTM inputs to reflect typical physiological and morphological characteristics of winter wheat canopies between BBCH stages 30 and 59 based on a comprehensive field phenotyping dataset described in Graf et al. (2023b). The leaf (PROSPECT-D) and canopy (4SAIL) input parameters including their range and distribution are shown in Table 3 based on Graf et al. (2023b). Following the proposed workflow by Graf et al. (2023b) we increased the physiological plausibility of RTM inputs. In detail, the leaf chlorophyll a+b and leaf carotenoid content were re-distributed based on empirical relationships between these traits and the GLAI established in Graf et al. (2023b) (GLAI - Cab relationship) and Wocher et al. (2020) (Cab - Car relationship). Using these relationships we can re-distribute Cab (through the canopy chlorophyll content) solely based on GLAI. Similarly, Car can be re-distributed solely based on Cab obtained in the previous step.

We run PROSAIL in forward mode based on the input parameters denoted in Table 3 for each S2 scene during the stem elongation period. Illumination and observer angles were set to scene-specific values obtained from the S2 scene metadata. In total, we run 50 000 PROSAIL simulations per S2 scene. The resulting spectra were converted to the spectral resolution of S2 by convolution of the original PROSAIL outputs in 1 nm spectral resolution with the spectral response functions of S2A and B provided by ESA[3]. In addition, we applied further physiological plausibility checks introduced by Wocher et al. (2020). In detail, we dropped simulated

[3] https://sentinel.esa.int/web/sentinel/user-guides/sentinel-2-msi/document-library/-/asset_publisher/Wk0TKajiISaR/content/sentinel-2a-spectral-responses

spectra with a shift of the green reflectance peak towards wavelengths shorter than 574 nm, which was considered implausible based on extensive survey of handheld and airborne hyperspectral imaging data of green vegetation. Around 10% of the simulated PROSAIL spectra were therefore discarded. The resulting spectra were stored in lookup tables (lookup-table (LUT)s) per S2 scene.

Table 3: Parameter ranges and distributions for the combined leaf (PROSPECT-D) and canopy (4SAIL) RTM (PROSAIL) for winter wheat canopies in the stem elongation phase. The ranges are given for uniform distributions (range) or a truncated Gaussian distribution with mean and standard deviation denoted in brackets. Cab and Car are redistributed on GLAI. All values and distributions are taken from Graf et al. (2023b).

| **Trait** | **Description** | **Unit** | **Range** |
|---|---|---|---|
| **PROSPECT-D (Leaf)** | | | |
| N | Leaf Structure Parameter | [-] | 1 - 2.5 (1.5, 0.2) |
| Cab | Leaf Chlorophyll a+b Content | $[\mu g\ cm^{-2}]$ | redistributed based on GLAI |
| Car | Leaf Carotenoid Content | $[\mu g\ cm^{-2}]$ | redistributed based on Cab |
| Cant | Leaf Anthocyanin Content | $[\mu g\ cm^{-2}]$ | 0.0 - 5.0 (2.0, 0.8) |
| Cbrown | Brown Pigments | [-] | 0 - 1 |
| Cw | Equivalent Water Thickness | [cm] | 0 - 0.07 (0.04, 0.02) |
| Dm | Dry Matter Content | $[g\ cm^{-2}]$ | 0 - 0.01 |
| **4SAIL (Canopy)** | | | |
| GLAI | Green Leaf Area Index | $[m^2\ m^{-2}]$ | 0.5-6.5 |
| ALA | Leaf Inclination Angle | [deg] | 30 - 70 |
| hspot | Hot spot Parameter | [-] | 0.01 - 0.5 |
| rsoil | Soil Brightness Factor | [-] | 0 - 1 |
| psoil | Dry/ Wet Soil Factor | [-] | 0 - 1 |

### *3.3.3. Radiative transfer model inversion*

For RTM inversion we used the PROSAIL spectra stored in LUTs per scene. We retrieved raw GLAI per S2 pixel by comparing S2-observed ($\rho_{S2}$) spectra with the

simulated spectra in the LUT ($\rho_{LUT}$) by means of the mean absolute error (MAE) for all $n$ S2-bands considered (i.e., $n = 9$) as suggested by Graf et al. (2023b).

$$MAE = \frac{1}{n} \sum_{i=0}^{n} |\rho_{S2_i} - \rho_{LUT_i}| \tag{2}$$

The median GLAI value obtained from the 5000 simulated spectra with the smallest MAE was then used as the S2-derived raw GLAI observation per S2 pixel.

### *3.4. Time series reconstruction*

#### *3.4.1. DRC-derived growth rates at the farm scale*

Fitted DRCs were applied to hourly and daily air temperature data at the validation sites (Section 2.2, Figure 2a). This converted each air temperature reading into a GLAI growth rate. Thus, per site and DRC GLAI growth rates in hourly and daily resolution were available.

#### *3.4.2. S2-derived raw GLAI observations at the pixel scale*

A simple outlier detection formalism was introduced to account for undetected atmospheric disturbances in the raw S2 GLAI observations (Figure 2b). Atmospheric disturbances usually cause negatively biased outliers in remotely-sensed trait observations (Chen et al., 2004). Therefore, raw S2 GLAI values of a pixel that deviated from the mean of all raw GLAI values by more than a single standard deviation in the negative y-direction were discarded. This did not apply to the first GLAI observation in time due to two reasons: First, we lack sufficient temporal context. Second, due to its proximity to the early phase of stem elongation a low GLAI value is physiologically plausible.

### *3.4.3. Data assimilation using Ensemble Kalman Filtering*

We aimed to combine the modelled DRC GLAI growth rates reflecting a-priori physiological knowledge about the relationship of growth to air temperature with raw S2 GLAI observations to obtain the best possible estimate of the effective GLAI (Figure 2c). Combining models with observations presents a data assimilation problem. In our case, we assimilated the raw S2 GLAI observations into the DRC-based GLAI growth rates to introduce spatial detail while retaining the high temporal resolution and physiological meaning of the underlying temperature data.

For data assimilation, the Kalman filter (KF) is widely used. In essence, KF is a sequential approach estimating the "true", hidden state vector of a system by updating the modelled states whenever an observation becomes available. In our case, the hidden state vector is given by the actual but unknown GLAI time series of a pixel. Since, both, the DRC models and the S2 observations have uncertainties, we use the probabilistic ensemble Kalman filer (EnsKF). The EnsKF allows to include model and observation uncertainty into the data assimilation process (Evensen, 2003). EnsKF frameworks have therefore been widely used in assimilating remotely sensed crop traits in crop models (de Wit and van Diepen, 2007; Zhao et al., 2013; Huang et al., 2016). Graf et al. (2023a) found that raw GLAI values derived from S2 take relative standard uncertainties up to 5% due to uncertainty in the S2 top-of-atmosphere reflectance data. For in-situ GLAI and temperature data we estimated a similar magnitude of uncertainty and set relative model uncertainty to 5%. The EnsKF ensemble size was set to 50 ensemble members to balance computational complexity with statistical significance as suggest by de Wit and van Diepen (2007)

and Zhao et al. (2013).

Figure 4 shows the proposed data assimilation approach, i.e., a zoom-in into Figure 4c, for a randomly selected S2 pixel at the Strickhof site in 2022. Figure 4a denotes the hourly air temperature time series available from the nearby weather station that was input into the DRCs to obtain hourly GLAI growth rates. The raw S2 GLAI observations (red dots) were assimilated into the DRC GLAI growth rates (Figure 4b) and subsequently used to reconstruct the final DRC GLAI time series with uncertainties (Figure 4c). Below we explain the steps in more detail.

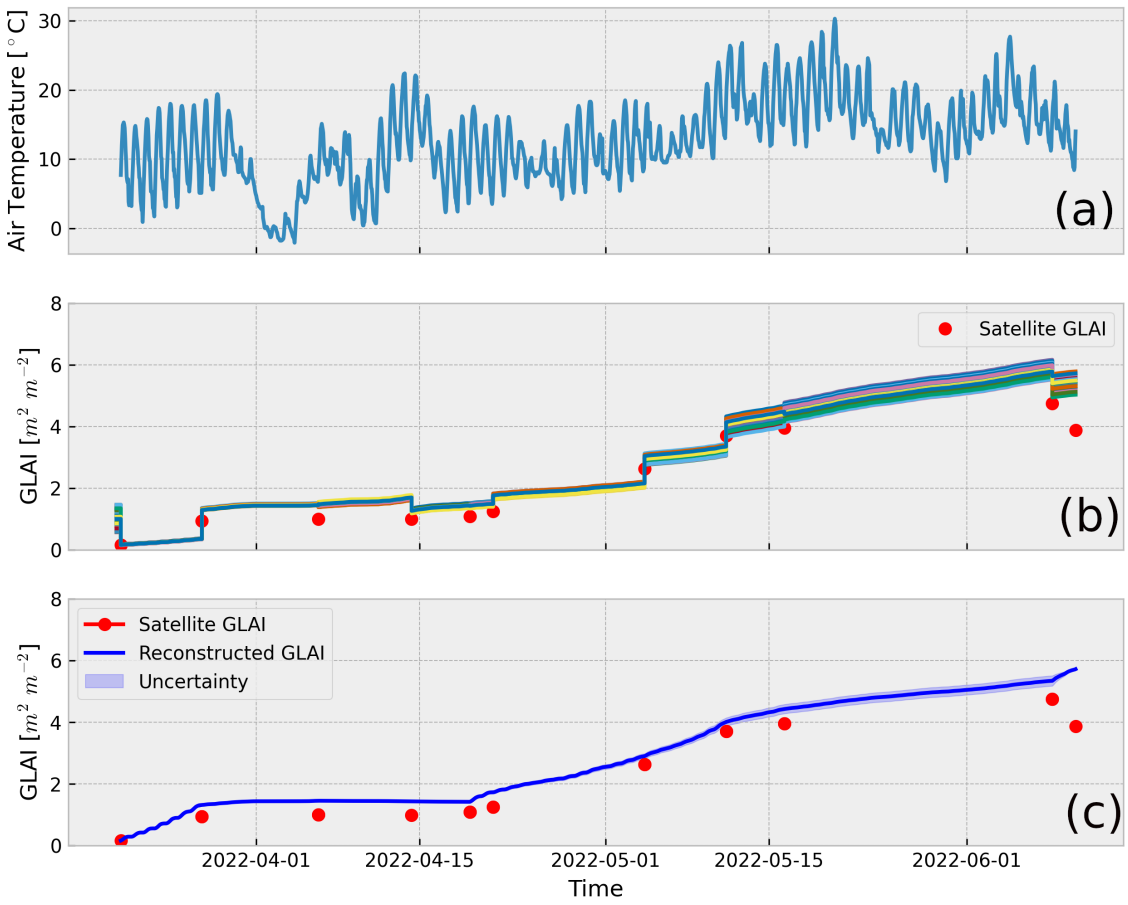


Figure 4: Example of the proposed probabilistic GLAI assimilation for a single S2 pixel at the Strickhof site in 2022 combining hourly air temperature data (a) with raw S2 GLAI observations (red dots) using DRC-based cumulative daily growth rates (solid colored lines in b) to reconstruct GLAI time series with associated uncertainties (c). The dose-response curve type used in this case was asymptotic.

As a first step, we performed a conventional EnsKF assimilation (Figure 4b) using DRC-based growth rates derived from air temperature time series (Figure 4a). As the DRCs provide growth rates, an initial GLAI must be provided. We therefore initialised each of the 50 ensembles by randomly sampling between the lower and upper GLAI bounds using a uniform probability distribution. The initial GLAI

bounds were set to a range of 0.5 to $1.5m^2\ m^{-2}$ based on empirical knowledge. We started the model runs just before the first S2 observation (Figure 4b, left). We then accumulated all the DRC GLAI growth rates up to the first raw S2 GLAI observation. At the time $t$ of the observation, we computed the Kalman gain $K$:

$$K = P_e H^T (H P_e H^T + R_e)^{-1} \tag{3}$$

In Equation 3, $P_e$ and $R_e$ denote the model and observation covariance matrices based on their uncertainties, and $H$ is the measurement operator which is the identity matrix since GLAI is directly observable. Using $K$, we calculate the Kalman innovation term $KI$

$$KI = D - (HA) \tag{4}$$

where $D$ denotes the observation matrix with uncertainties and $A$ is the matrix with modelled GLAI values at time $t$. Thus, the model state at the analyses step $A^a$ can be obtained:

$$A^a = A + K\ KI \tag{5}$$

$A^a$ re-initializes the ensembles at $t$. As before, we then calculated the cumulative DRC growth rates until the next raw S2 GLAI observation at time $t+1$. At $t+1$ a new $A^a$ was calculated using Equations 3 to 5. This procedure was repeated for all S2 observations except the last one as shown in Figure 4b.

Here, a limitation of the EnsKF method becomes clear: EnsKF is a non-conservative

approach, i.e., potentially large jumps in the modeled time series are caused by the assimilation (Figure 4b). This is physiologically implausible, since GLAI trajectories must be continuous. Therefore, we had to extended the EnsKF approach in a second step:

We addressed said problem by replacing the raw S2 GLAI observations with the ensemble mean at each analysis step $A^a$ ($GLAI_{assim}$). This is to ensure that model and observation information is preserved. The ensemble standard deviation is retained as a measure of uncertainty, taking into account both, model and observation uncertainty. Using the $GLAI_{assim}$ values, we used the DRCs for a second time to model growth. This time, however, we used the DRCs to interpolate between the $GLAI_{assim}$ values, which are still temporally sparse. We scaled the cumulative growth rates to exactly match the $GLAI_{assim}$ values. In case $GLAI_{assim_{t+1}}$ was smaller than $GLAI_{assim_t}$, $GLAI_{assim_{t+1}}$ was discarded. In this case, we interpolated between $GLAI_{assim_t}$ and $GLAI_{assim_{t+2}}$. This ensured that undetected outliers in the raw S2 GLAI values were not given too much weight, while preserving medium range temporal characteristics. The resulting interpolated GLAI curve at the temporal resolution of the DRC (i.e., hourly or daily) is shown in Figure 4c, in which the solid blue line denotes the assimilated, DRC-interpolated reconstructed GLAI time series.

From here on we name the reconstructed time series after the underlying DRCs. That is, by "non linear" we mean from now on the EnsKF assimilated and interpolated data points created using the non linear DRC and raw S2 GLAI observations. The same applies to "asymptotic" and "Wang Engels".

### *3.4.4. Baseline method*

As baseline method, a sigmoid (a.k.a. logistic) function was fitted to the same raw S2 GLAI observations at the pixel scale (Figure 2d). Due to its S-shaped form, sigmoid functions are widely used in remote sensing to obtain continuous time series of vegetation traits. The sigmoid function is a simplified version of DL (Beck et al., 2006), which only accounts for the generative (ascending) branch of GLAI development. It is therefore a baseline that, unlike other statistical models such as the Savitzky-Golay filter, already has parameters with a certain biological significance.

The sigmoid function takes four parameters: The supremum of the function's values $L$, the growth rate $k$, the function's midpoint $x_0$ and an offset from zero $b$ which is necessary because GLAI values around BBCH 30 are usually larger than zero:

$$f(x) = \frac{L}{1 + e^{-k(x-x_0)}} + b \tag{6}$$

A minimum of four raw S2 GLAI observations are required to fit the model parameters. We fit the sigmoid function to each pixel, taking into account all available GLAI observations, using the Levenberg-Marquardt algorithm available in the scipy Python library (version 1.11.0) with the function "scipy.optimze.curve_fit". The maximum number of optimisation steps was set to 1000. The parameterised logistic function (equation 6) was then used to reconstruct the GLAI time series at daily resolution. We will refer to this time series as the baseline GLAI.

### *3.5. Model Validation*

The raw S2 GLAI observations and the reconstructed continuous DRC and baseline GLAI time series were compared against the independent in-situ validation GLAI data (Section 2.2). We obtained matching tuples of reconstructed and in-situ GLAI by time stamp and spatial intersection of the sampling points with the S2 10 m pixel grid. In the case of the reconstructed time series (i.e., DRC and baseline GLAI), each in-situ GLAI value could be matched to a modelled GLAI value as the time series is continuous and spans the whole time period for which in-situ data was available. For the raw S2 GLAI observations this was not the case due to the aforementioned temporal sparsity of the satellite observations. Therefore, we only used in-situ GLAI values that had a satellite overpass with a maximum difference of one day.

Comparison was carried out by means of common error measures of the linear regression between modelled and observed values. Error measures included the RMSE, normalized RMSE (nRMSE), Pearson's R-square ($R^2$), and bias between reconstructed ($GLAI_{reconstructed}$) and in-situ GLAI values ($GLAI_{insitu}$). The bias was calculated using the variance of $GLAI_{reconstructed}$ ($var(GLAI_{reconstructed})$) and the mean of the squared differences ($MSD$) between mean $GLAI_{reconstructed}$, $\mu(GLAI_{reconstructed})$, and $GLAI_{insitu}$ considering all $n$ matching tuples available:

$$MSD = \frac{1}{n}\sum_{i=0}^{n}(\mu(GLAI_{reconstructed}) - GLAI_{insitu_i})^2 \tag{7}$$

$$Bias = MSD - var(GLAI_{reconstructed}) \tag{8}$$

Error statistics were produced for all sites and years as well as for single sites, years

and BBCH macro stages (i.e, BBCH 30-39, 50-59) to assess model performance in space, time, and with respect to phenological development. In addition, we visualized the temporal trajectories of GLAI per parcel to evaluate the physiological plausibility and consistency of the reconstructed GLAI time series.

## 4. Results

### *4.1. Validation of raw S2 GLAI observations against in-situ GLAI*

Figure 5 shows the raw S2 GLAI observations plotted against in-situ measured GLAI with a maximum temporal offset of one day. The RMSE was about 1.16 $m^2$ $m^{-2}$ (nRMSE 18.92%) with a bias of 1.87 $m^2$ $m^{-2}$. The raw S2 GLAI observations explained 64% of the variability in the in-situ values. The raw S2 GLAI values showed a clear underestimation of in-situ GLAI $> 5$ $m^2$ $m^{-2}$ in 2022 (blue dots in Figure 5) as well as three isolated outliers in 2023 (cross markers) for in-situ GLAI values between 2 and 3 $m^2$ $m^{-2}$. Due to high cloud cover, only 8 out of 55 available observations for validation were recorded in 2023. Therefore, no year effects could be studied. The same applies to the phenological macro-stages for which not enough data was available to compute robust error statistics.

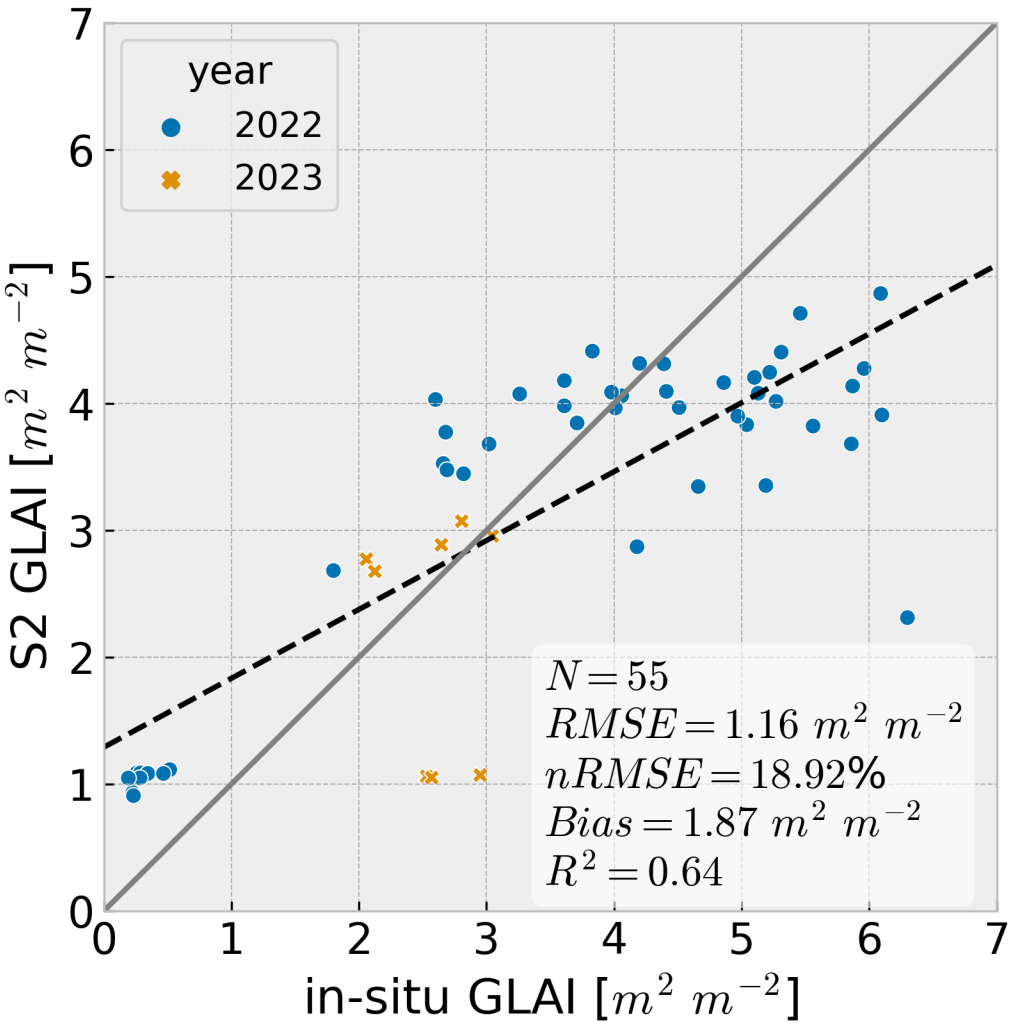


Figure 5: Scatter plots of S2 observed and in-situ measured GLAI at the validation sites using data from 2022 and 2023. The oblique solid lines denotes the desired 1:1 fit; the dashed line denotes the linear regression line between S2 observed and in-situ measured GLAI values. N = 55. The years are color-coded.

### *4.2. Validation of reconstructed GLAI time series against in-situ GLAI*

Similar to Figure 5, scatter plots of reconstructed GLAI (i.e., DRC and baseline GLAI) at hourly and daily resolution against in-situ measured GLAI are displayed

in Figure 6 (N = 178). Figure 6 (a-c) shows the results of the proposed DRC GLAI time series, and (d) the baseline GLAI results which are available in daily resolution, only. The error statistics are listed in Table 4.

All models revealed a tendency to overestimate low in-situ GLAI ($< 1.0\ m^2\ m^{-2}$). The baseline (Figure 6d) clearly underestimated in-situ GLAI values $> 5.0\ m^2\ m^{-2}$. All models performed similar in terms of RMSE, nRMSE and $R^2$ (Table 4). The hourly asymptotic DRC GLAI had the smallest RMSE ($0.98\ m^2\ m^{-2}$) closely followed by the daily asymptotic and non linear DRC GLAI (RMSE around $0.99\ m^2\ m^{-2}$, nRMSE around 15%). The highest RMSE was observed for the Wang Engels DRC GLAI at hourly resolution ($1.12\ m^2\ m^{-2}$, nRMSE: 17.43%). The baseline GLAI had a slightly lower RMSE ($1.05\ m^2\ m^{-2}$, nRMSE: 16.27%) than the daily Wang Engels DRC GLAI ($1.06\ m^2\ m^{-2}$). A similar picture revealed $R^2$ which ranged between 0.54 (Wang Engels hourly DRC GLAI) and 0.70 (non linear daily DRC GLAI). The highest bias was observed for the baseline GLAI ($1.66\ m^2\ m^{-2}$). This was higher than for the DRC GLAI and more than two times larger than the smallest bias ($0.73\ m^2\ m^{-2}$) obtained from the hourly Wang Engels DRC GLAI which had the lowest bias.

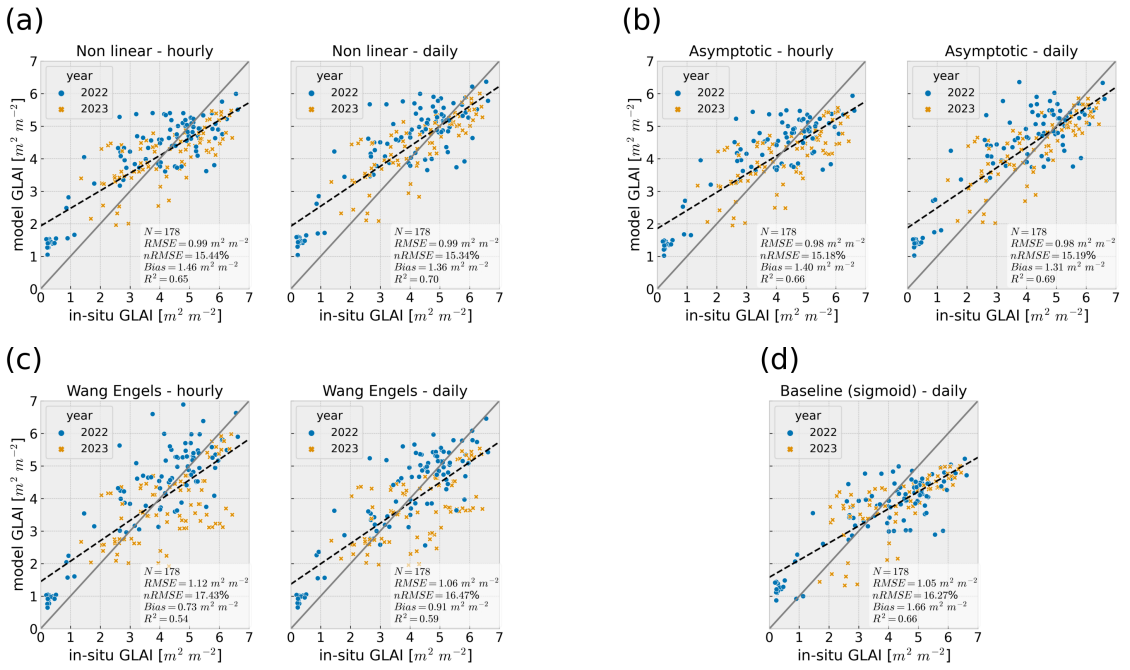


Figure 6: Scatter plots between reconstructed DRC (a-c) and baseline (d) GLAI and in-situ GLAI at the validation sites using data from 2022 and 2023 (color-coded). For each DRC GLAI, the results using hourly and daily mean air temperature are shown (a-c). The baseline GLAI is only available in daily resolution (d). The oblique solid line denotes the desired 1:1 fit and the dashed line the linear regression line between reconstructed and in-situ GLAI values. N = 178.

Table 4: Error statistics of reconstructed and in-situ GLAI values (N = 178). RMSE and bias are given in $m^2$ $m^{-2}$, nRMSE in percent and $R^2$ is dimensionless.

| model | resolution | RMSE | nRMSE | Bias | $R^2$ |
|---|---|---|---|---|---|
| Non linear | hourly | 0.99 | 15.44 | 1.46 | 0.65 |
| | daily | 0.99 | 15.34 | 1.36 | 0.70 |
| Asymptotic | hourly | 0.98 | 15.17 | 1.40 | 0.66 |
| | daily | 0.98 | 15.19 | 1.31 | 0.69 |
| Wang Engels | hourly | 1.12 | 17.43 | 0.73 | 0.54 |
| | daily | 1.06 | 16.47 | 0.91 | 0.59 |
| Baseline (sigmoid) | daily | 1.05 | 16.27 | 1.66 | 0.66 |

*4.2.1. Effect of the years*

Error statistics by year are shown in Table 5. Arrows in table indicate whether a metric value remain unchanged (→), decrease (↓), or increased (↑) from 2022 to 2023. For all models and temporal resolutions, the relative error was higher and $R^2$ lower in 2023 (N = 82) than 2022 (N = 96). In 2022, nRMSE values ranged from 13.04 (Wang Engels daily) to 16.72% (non linear daily), while $R^2$ took values between 0.74 (baseline) and 0.8 (Wang Engels daily). In 2023, nRMSE values were in the range between 17.16 (asymptotic daily) and 25.62% (Wang Engels hourly) with $R^2$ between 0.3 (Wang Engels hourly) and 0.62 (non linear daily). The RMSE was higher in 2023 than 2022 in four cases (asymptotic hourly, Wang Engels hourly and daily, and the baseline), unchanged in one case (non linear hourly), and decreased in the remaining two cases (non linear daily and asymptotic daily). The highest RMSE

was obtained from the hourly Wang Engels DRC in 2023 (1.30 $m^2$ $m^{-2}$, value in 2022: 0.94 $m^2$ $m^{-2}$), the lowest for the Wang Engels DRC in 2022 (0.84 $m^2$ $m^{-2}$, value in 2023: 1.27 $m^2$ $m^{-2}$). The bias decreased in all cases in 2023 compared to 2022 except the Wang Engels DRC: Here, the bias increased from 0.83 to 1.10 $m^2$ $m^{-2}$ (hourly) and from 0.90 to 1.22 $m^2$ $m^{-2}$ (daily).

Table 5: Error statistics of reconstructed and in-situ GLAI values in 2022 (N = 96) and 2023 (N = 82). The arrows indicate the change in the metrics from 2022 to 2023: ↑ means the value increased in 2023 compared to 2022, ↓ it decreased, and → it remained unchanged. RMSE and bias are given in $m^2$ $m^{-2}$, nRMSE in percent and $R^2$ is dimensionless.

| model | resolution | RMSE | | | nRMSE | | | Bias | | | $R^2$ | | |
|---|---|---|---|---|---|---|---|---|---|---|---|---|---|
| | | 2022 | 2023 | | 2022 | 2023 | | 2022 | 2023 | | 2022 | 2023 | |
| Non linear | hourly | 0.99 | 0.99 | → | 15.44 | 19.58 | ↑ | 1.71 | 1.18 | ↓ | 0.75 | 0.49 | ↓ |
| | daily | 1.07 | 0.87 | ↓ | 16.72 | 17.18 | ↑ | 1.64 | 1.01 | ↓ | 0.75 | 0.62 | ↓ |
| Asymptotic | hourly | 0.96 | 0.99 | ↑ | 14.98 | 19.52 | ↑ | 1.66 | 1.14 | ↓ | 0.77 | 0.50 | ↓ |
| | daily | 1.06 | 0.87 | ↓ | 16.47 | 17.16 | ↑ | 1.60 | 0.96 | ↓ | 0.75 | 0.60 | ↓ |
| Wang Engels | hourly | 0.94 | 1.30 | ↑ | 14.64 | 25.62 | ↑ | 0.83 | 1.10 | ↑ | 0.77 | 0.30 | ↓ |
| | daily | 0.84 | 1.27 | ↑ | 13.04 | 25.02 | ↑ | 0.90 | 1.22 | ↑ | 0.80 | 0.33 | ↓ |
| Baseline (sigmoid) | daily | 1.03 | 1.07 | ↑ | 15.97 | 22.55 | ↑ | 1.96 | 1.21 | ↓ | 0.74 | 0.48 | ↓ |

*4.2.2. Effect of phenology*

The GLAI reconstruction errors were dependent on the phenological macro-stage. Figure 7 shows the error measures for BBCH macro stages 30-39 (stem elongation), and 50-59 (heading) for the DRC and baseline with daily GLAI output. There were

too few in-situ data for the booting stage (N = 5) available, so we restricted our analysis to stem elongation (N = 136) and heading (N = 37). For these stages, the baseline GLAI exhibited the largest bias (1.6 and 1.2 $m^2$ $m^{-2}$, respectively). During heading, the baseline GLAI also showed largest RMSE (around 1.2 $m^2$ $m^{-2}$) and its bias was almost twice as high as in the DRC GLAI (bias around 0.6 $m^2$ $m^{-2}$). The difference in $R^2$ was less pronounced; the DRC and baseline GLAI had a high $R^2$ in stem elongation (0.55 to 0.73), which decreased significantly during heading (0.05 to 0.15). Overall, the differences between the three DRC GLAI models were less pronounced than the difference between these models and the baseline GLAI.

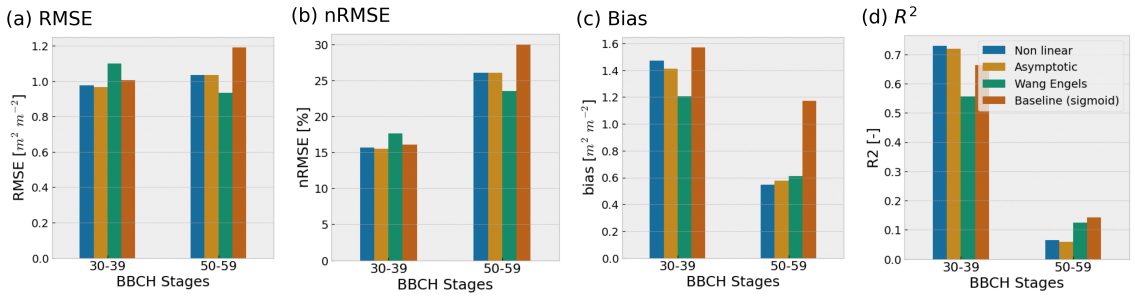


Figure 7: Reconstructed versus in-situ GLAI error statistics per BBCH macro-stage and model. Only the results of the daily DRC GLAI are shown.

### *4.2.3. Time series reconstruction*

Figure 8 visualizes the reconstructed median DRC and baseline GLAI time series at daily resolution in days after sowing (DAS) per field parcel and year (see also Figure 1). The spatial in-field variability obtained from each model is shown as filled areas color-coded by model. The in-situ GLAI values are plotted as blue dots to allow comparison of reconstructed versus measured in-field heterogeneity and temporal dynamics. Both, DRC and baseline GLAI show an increase in GLAI from

the beginning of the stem elongation to the end heading, which largely reflects the dynamics of the in situ data.

The asymptotic (dotted green) and non linear (solid golden) DRC GLAI were able to accurately reconstruct in-situ GLAI spatial variability and reflect the temporal trajectories of the in-situ GLAI values. These models were able to represent the higher in-situ GLAI ($> 5\ m^2\ m^{-2}$) during late booting and heading. Wang Engels DRC GLAI (dash-dotted brown) mostly followed similar trajectories but with a tendency towards a delayed increase in GLAI evident in the 2023 plots (Figure 8e-g). In addition, the Wang Engels DRC GLAI showed a less smooth progression than the other two DRC GLAI models and the baseline, as evidenced by jumps and plateaus in the median GLAI time series (Figure 8).

The baseline GLAI (dashed blue) showed the expected smooth progression. While in-situ GLAI at the beginning and middle of the time series are still reproduced largely accurately, the underestimation of higher in-situ GLAI values ($>5\ m^2\ m^{-2}$) is clearly evident in Figure 8. In Figure 8g, the baseline GLAI also revealed a rapid increase in GLAI between DAS 160 and 180 from 0.5 to 3.5 $m^2\ m^{-2}$ which is not present in the DRC GLAI time series.

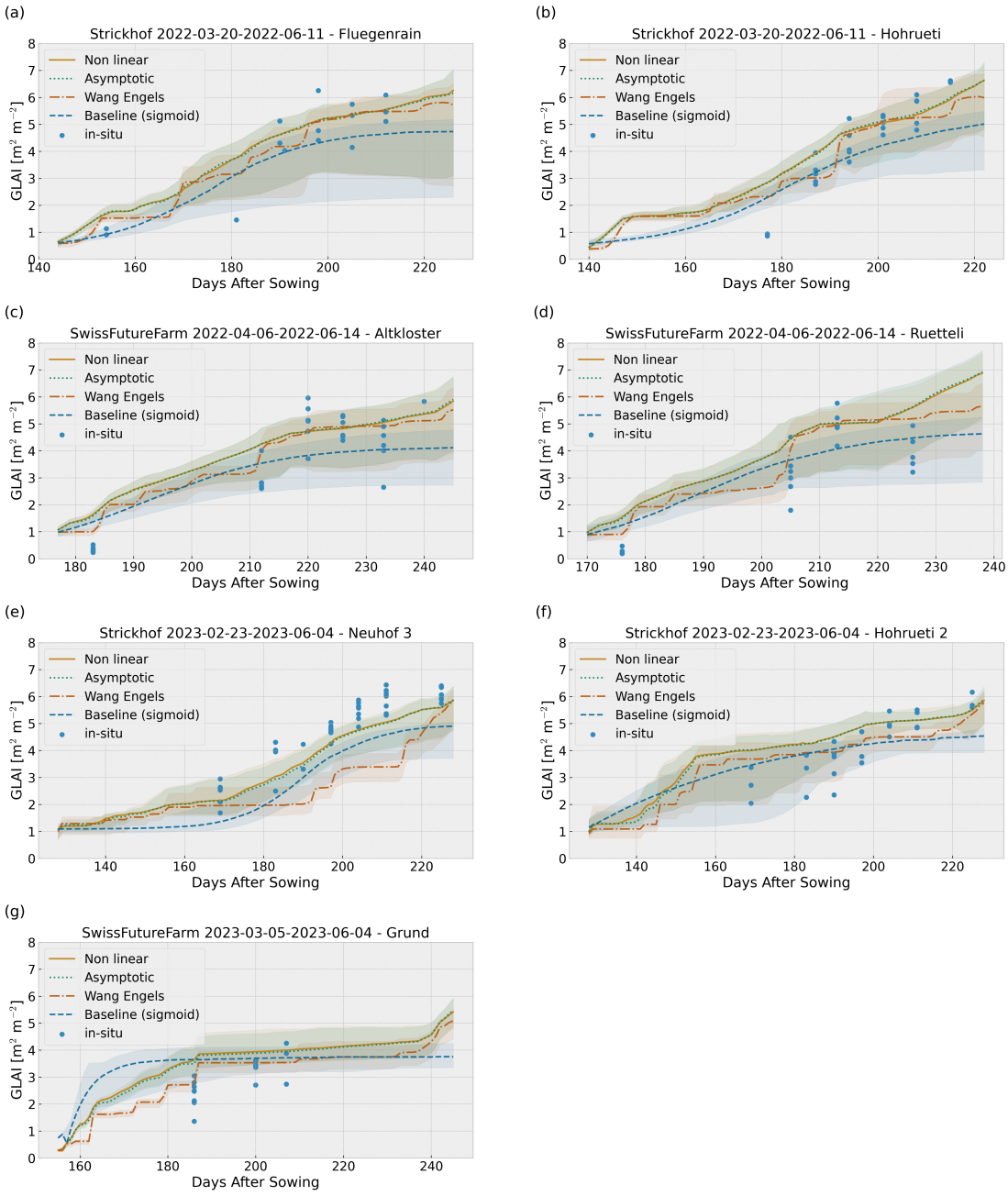


Figure 8: Median daily reconstructed DRC and baseline GLAI time series (lines) and spatial in-field variability in terms of the 5% to 95% percentile spread (filled areas) at the field parcels of the validation site (Figure 1). The in-situ GLAI values are denoted as blue dots.

To further highlight the difference between the DRC and the baseline GLAI, we plotted the daily asymptotic DRC GLAI which achieved overall high accuracy (see Tables 4-5), against the baseline GLAI considering all pixels and dates. The resulting scatter plots are shown for each validation site and year in Figure 9. In Figure 9a-c it becomes clear that the baseline GLAI reconstructed slightly lower GLAI values than the asymptotic DRC. The effect was particularly pronounced for GLAI values $> 5\ m^2\ m^{-2}$, as shown by the systematic deviation from the 1:1 line. In Figure 9d the effect is less pronounced. This site (Swiss Future Farm 2023), however, was also affected by a high proportion of pixels that could not be reconstructed in the baseline GLAI, as we will show in the next section.

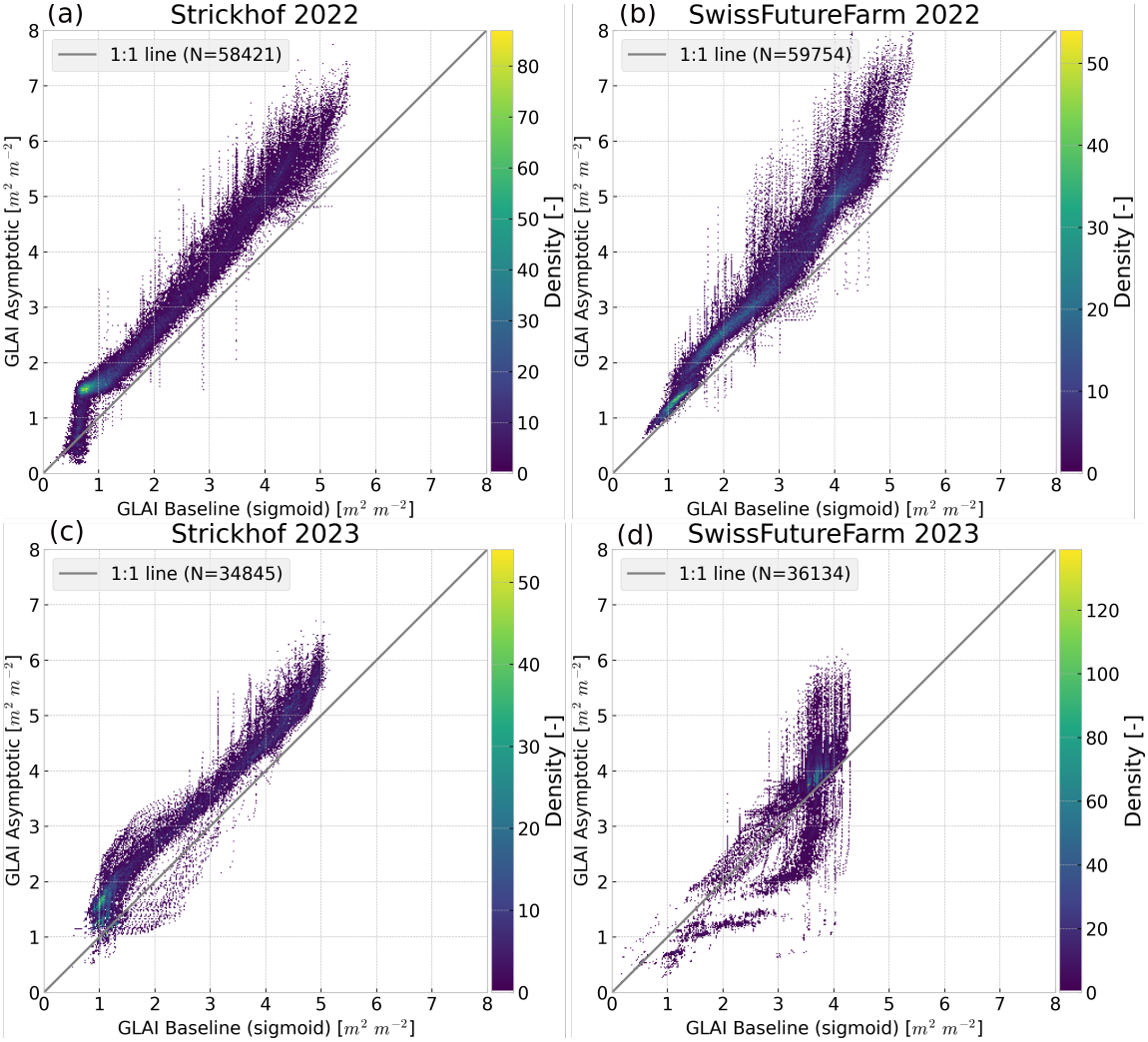


Figure 9: Intercomparison of reconstructed GLAI time series values at the Strickhof and Swiss Future Farm sites in 2022 (a, b), and 2023 (c, d), respectively, showing all reconstructed GLAI values from the asymptotic DRC GLAI plotted against all reconstructed baseline GLAI values.

### *4.3. GLAI reconstruction success rate*

As described in Section 3.4.4, the baseline requires at least four valid raw S2 GLAI values to estimate the function parameters. However, this requirement was not met for all S2 pixels: While the overall number of S2 observations is higher than

four at all sites (see Section 2.3), the SCL and simple outlier filtering (Section 3.4.2) caused the total number of valid raw GLAI observations to drop below the threshold of four in some cases. Overall, the baseline GLAI could not be fitted to 12.43% of the pixels at the validation sites, with variations from 5.46% at the Swiss Future Farm in 2022 to 20.08% at the same site in 2023. The latter case is displayed in Figure 10 comparing the daily asymptotic DRC GLAI to baseline GLAI for two dates during late stem elongation and heading. The failure of the baseline to reconstruct GLAI values was caused in two thirds of the pixels by a too low number of valid raw GLAI observations ($< 4$), and in one third by the non-convergence of the optimization algorithm after reaching the maximum number of iterations (1000). Although often only pixels at the parcel boundaries were affected, about 40% of the pixels were located within the parcels, resulting in undesired spatial gaps in the reconstructed baseline GLAI (c.f., Figure 10, right). In contrast, for the DRC GLAI, which only require a minimum number of two valid GLAI observations, reconstruction could be performed for all S2 pixels.

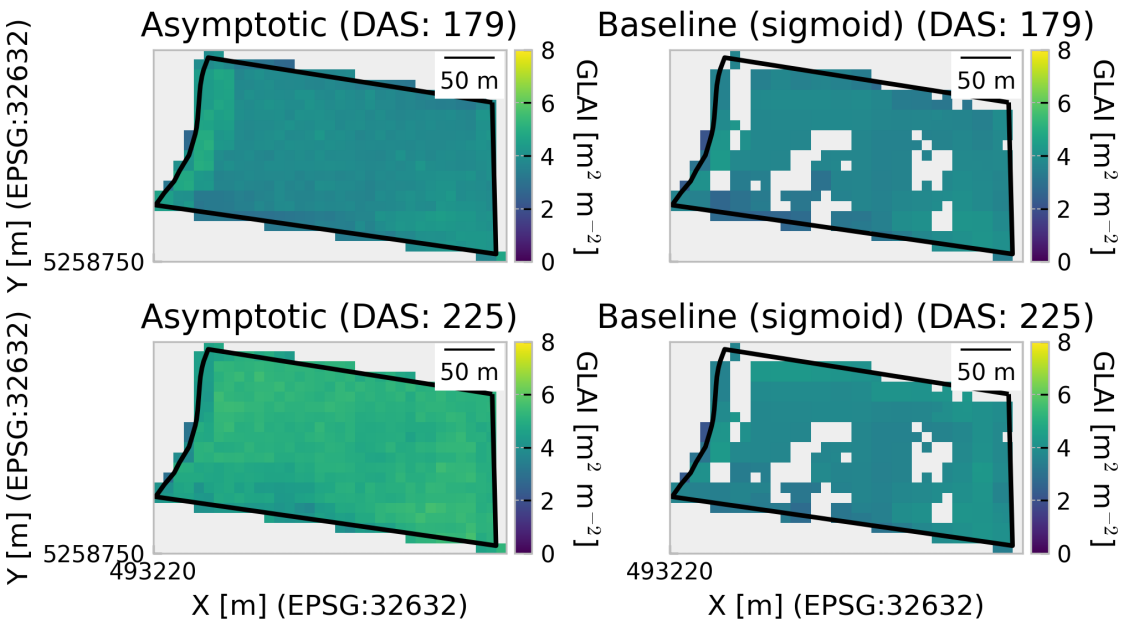


Figure 10: Maps of daily asymptotic DRC (left) and baseline GLAI (right) for the parcel Grund at Swiss Future Farm in 2023 for two dates during late stem elongation (top) and heading (bottom) expressed as days after sowing (DAS). The parcel boundary is shown as black line.

## 5. Discussion

### *5.1. Time series reconstruction accuracy and plausibility*

Although the raw GLAI values and the reconstructed GLAI are not directly comparable due to the different number of data points, we conclude that the reconstructed GLAI values using DRCs and the baseline reduced the GLAI retrieval error (Figures 5 and 6). This was mainly due to the removal of outliers in the negative y-direction caused by atmospheric perturbations, suggesting that both the DRC and baseline approaches dealt reasonably well with the effects of undetected clouds and cloud shadows. Nevertheless, a systematic underestimation of GLAI values greater than 5 $m^2$ $m^{-2}$ was observed for the GLAI baseline. This underestimation was hardly

noticed in the proposed reconstruction with DRCs (see Figure 6) as the DRC GLAI was mostly higher than the baseline (Figures 8 and 9). The underestimation of S2 GLAI observations was probably due to the RTM inversion approach used: It is a known problem that RTMs such as PROSAIL exhibit saturation phenomena at high biomass levels due to leaf clumping (Richter et al., 2011). As the baseline only uses the raw S2 GLAI observations, the fit could not compensate for saturation effects, so the reconstructed time series consequently underestimated GLAI. In addition, the sigmoid fit aims to minimise the mean error of the reconstructed curve to the raw S2 GLAI observations. This may lead to further underestimation of GLAI values, as the reconstructed curve may sometimes be lower than the underlying S2 GLAI observations.

In the case of DRCs, the assimilation scheme integrates two data sources with distinct advantages: The DRCs contain prior physiological knowledge about the relationship between air temperature and growth, thereby mitigating the underestimation of GLAI values as this relationship was established using high-quality in-situ data. The raw S2 GLAI provides spatial details that are absent from the temperature data. This makes the approach well-suited for fine-grained spatial growth analysis. In addition, as air temperature records are usually continuous, the GLAI reconstruction between S2 observations relies on encoded physiological knowledge, reducing the likelihood of unrealistically fast growth rates due to physiological constraints imposed by the temperature. It is not ensured that the baseline will accurately reflect the prevailing conditions. This is due to the fact that reconstruction between S2 observations solely relies on the function parameters, which do not necessarily contain

sufficient information about the underlying biological mechanisms. Consequently, the baseline might indicate high growth rates even if the temperature is significantly below or above the critical $T_{min}$ and $T_{max}$ thresholds.

The accuracy of the DRC-reconstructed GLAI was comparable to approaches using more complex mechanistic crop growth models, which require a significantly higher number of parameters: Ma et al. (2022) reported values of $R^2$ between 0.7 and 0.73 for winter wheat in northern China (relative errors between 22 and 26%) using the SAFYE crop growth model in combination with S2 images for two growing seasons. This is comparable to the accuracy using DRCs (Table 4). Higher accuracy was reported by Hank et al. (2015) for winter wheat in southern Germany. They achieved a root mean square error of 0.35 $m^2$ $m^{-2}$ ($R^2$ 0.96) using a more complex crop growth model combined with Landsat and RapidEye satellite remote sensing data. However, their sample size was small (N = 19) and included only a single growing season and field parcel. Even smaller errors were reported by Zhang et al. (2021) (relative errors between 2.0 and 9.2%) using SAFYE for two growing seasons of winter wheat in central China. Instead of using satellite imagery, they used GLAI retrieved from handheld hyperspectral data, which is arguably not comparable to space-borne GLAI retrieval. However, more complex crop growth models often aim to model phenology or even yield, whereas the approach presented is designed to interpolate GLAI observations in a physiologically meaningful way. This also means that the reduced complexity, and perhaps accuracy, can be compensated for by using the GLAI observations as guidance over the growing season.

However, the DRC approach is also likely to be limited by the lack of spatial

detail during long periods without S2 passes due to cloud cover – a problem shared with more complex crop growth models. Assimilation includes information on crop growth that has causes other than temperature alone, such as differences in soil properties or subtle differences in management. Without regular assimilation, this information cannot be incorporated into the DRC growth rates, limiting the accuracy of comparing the reconstructed GLAI with in-situ data. Therefore, a higher number of S2 observations is likely to result in higher reconstruction accuracy. This means that increasing the number of observations, e.g. by fusing GLAI from cube satellite constellations as suggested by Sadeh et al. (2021), could further increase the reconstruction accuracy. This method has two major drawbacks: First, the amount of data and model complexity increases significantly due to the addition of a second satellite platform. One of the main advantages of the DRC approach, however, is its simplicity. Secondly, most cube satellite constellations, unlike S2, are commercial products that carry a financial burden that not all users of remote sensing data may be able to bear. Still, as the question of the optimal number of satellite observations and their temporal distribution for data assimilation does not seem to have been conclusively clarified, there is potential for further research.

Of the three DRCs utilised, Wang Engels exhibited minimal bias, albeit the most inconsistent year-on-year outcome (see Tables 4-5). This is significant as the Wang Engels DRC has the most physiological significance, thereby making it a suitable candidate to examine the impact of rising temperatures and stress factors in the study area (Tschurr et al., 2020). Since there is a lack of additional in-situ GLAI data, the optimal approach was to optimize the Wang Engels DRC using only three

parameters. However, with additional data at hand, the year-to-year error could potentially decrease by optimizing an extra parameter without overfitting the data. In order to achieve this, a scaling parameter could be integrated, offering another degree of freedom to optimize $T_{base}$, $T_{opt}$, and $T_{max}$. Consequently, the Wang Engels DRC GLAI's performance could possibly be enhanced with more calibration data accessible. For now, the asymptotic DRC seems to be the most suitable choice: It is more sophisticated and marginally more precise than the nonlinear DRC. Moreover, its year-to-year performance is steady. Again, it is worth mentioning that additional in-situ calibration data from other environments (site-year combinations) would be advantageous for making a conclusive statement about selecting the DRC and studying the year-to-year performance and performance within selected phenological stages (Figure 7).

Concerning the selection of the temporal resolution of the air temperature data, our results did not reveal any pronounced tendency (see Table 4). Finer resolved covariate measurements could theoretically offer more information and therefore enhance growth prediction accuracy from a physiological standpoint. However, daily air temperature data is more accessible and requires fewer computational resources from an operational perspective. Overall, a conclusive answer to the second research question cannot be provided. Considerations related to physiology suggest that the use of hourly air temperature data is more favorable than daily data. As argued before, further calibration and validation data would be necessary to arrive at a conclusive statement.

### *5.2. Time series reconstruction stability*

The baseline GLAI resulted in up to 20% of pixels for which no GLAI time series could be reconstructed (Figure 10). This is due to the lack of a sufficient number of raw S2 GLAI observations or non-convergence of the optimiser (Levenberg-Marquardt, section 4.3). Increasing the number of iterations could counteract the non-convergence problem. The choice of the initial guess is also important for the successful and fast convergence of the optimiser. Still, there is no guarantee that the optimiser will converge and find a global minimum.

It could be argued that the absence of up to 20% of pixels might not significantly impact the results of aggregate statistics (such as median GLAI values per field parcel) in large-scale analyses where sub-field heterogeneity is negligible. However, we maintain that two issues persist.

First and foremost, spatial gaps in the reconstructed GLAI may result in inadequate sub-field scale analyses, particularly for precision farming applications. The same applies to small-scale farming systems with small field sizes ($< 1$ ha), for which the share of missing pixels might easily reach up to 100% due to the small number of S2 pixels covering a parcel.

Secondly, there are significant gaps within the field that are frequently the result of single observations being masked out by scene pre-classification. As previously discussed, the S2 SCL typically proves unreliable in accurately delineating clouds and shadows. Therefore, atmospheric disturbances may well have affected the neighbouring pixels, for which GLAI reconstruction proved successful from a technical point of view. Still, the pixels may exhibit physiologically implausible growth patterns as

a result of the partially degraded quality of the original S2 GLAI observations. The degenerated quality of the input data cannot be sufficiently compensated without the corrective effect of the DRC-based growth curves. We maintain that our suggested method surpasses statistical time series reconstruction in terms of reliability, as stated in our second research question.

### *5.3. Implications for crop productivity assessment*

The underestimation of GLAI values by the baseline has significant consequences for the assessment of crop productivity based on remote sensing, which often relies on methods similar to the baseline (Kooistra et al., 2023). This issue is exemplified by gross primary productivity (GPP), an indicator of energy fixed by photosynthesis minus losses through photorespiration (Hilty et al., 2021), which is also used on a global scale to study the effects of climate change on plant growth (Campbell et al., 2017). To estimate crop canopy GPP from remote sensing data, light use efficiency (LUE) models are often used (Dong et al., 2017, for instance). These models describe the efficiency with which photosynthetically active solar radiation (PAR) is converted into photosynthesis. As Monsi and Seaki (2004) demonstrated, the fraction of PAR intercepted by a canopy is linearly correlated with GLAI. Thus, according to Gitelson et al. (2015), precise estimates of LUE and GLAI are crucial for accurate estimation of GPP at canopy level. If maximum GLAI values are systematically underestimated, as in the case of raw and baseline GLAI, this could potentially affect the determination of GPP. To improve the accuracy and reliability of remotely sensed GPP estimates, our proposed method may be suitable. However, it is important to remember that GPP estimates do not only depend on GLAI and that the linear rela-

tionship between light interception and GLAI only holds true under the assumption of an idealized turbid medium which might fail for heterogeneous canopies (Hilty et al., 2021). Therefore, a more detailed assessment would be required to provide a quantitative estimate of the impact of underestimated GLAI on estimates of GPP or biomass. However, this is beyond the scope of this paper and should be addressed in further research.

In addition, the probabilistic data assimilation scheme accounts for model and data uncertainties, resulting in improved accuracy. The quantification of uncertainty is critical because it allows users to determine the suitability of a data product, such as the reconstructed GLAI time series, for a particular purpose, such as yield estimation as a measure of crop productivity. This information is not available from the baseline. In addition, the reported uncertainty can be transferred to derived products, adding further value. This is important in the context of decision support for adaptive crop management and could lead to more informed agricultural decision making (Meenken et al., 2021).

### *5.4. Ways forward*

The utilisation of prior knowledge about physiological processes holds the potential to enhance contemporary agricultural remote sensing methods. To bolster the reliability of our presented model, expansion of the calibration dataset to encompass more environments would be advantageous. This up-scaling would augment our ability to establish the temperature bounds ($T_{min}$ and $T_{max}$) which regulate crop growth. This is especially important in the case of more advanced DRCs like Wang Engels, which revealed promising performance due to its low bias (Table 4). Fur-

thermore, the dataset at hand demonstrated an imbalance in the measurements per site, which could potentially impact the final results. The absence of publicly accessible in-situ records evaluating phenology, GLAI measurements, and temperature is preventing the expansion of the dataset at present. Nevertheless, the ground truth data proved adequately representative to parameterise the DRC curves shown and to outperform the baseline method. As a result, we propose that upcoming field trials should include phenology and a minimum of environmental variables, along with functional crop characteristics, to facilitate development of physiological models. This will enable more rigorous parameter optimization and lead to a reduction in RMSE. Furthermore, it may be possible to estimate traits like yield while avoiding the use of complex crop growth models.

Regarding phenology, the approach could be expanded to encompass the entire phenological development cycle of wheat. In order to achieve this, sufficient calibration data is required for the phenological macro-stages preceding and following the stem elongation period, including the tillering or senescence phase. A phenology model is thus necessary for determining the timing and duration of phenological development stages. Such a phenology model should ideally describe the entire phenology using a simple and easily applicable approach, such as the DRC, which can even combine multiple environmental parameters.

Additionally, meteorological drivers of crop growth, such as vapor-pressure-deficit (VPD) or global radiation, could be included, apart from temperature. These meteorological parameters, however, present greater difficulty in terms of measurement and acquisition. Our proposal utilises air temperature as a readily available meteoro-

logical metric, which not only simplifies the approach but also renders it potentially implementable on a global scale. Furthermore, this modelling approach using DRC curves can also be applied to other crops (Parent and Tardieu, 2012; Roth et al., 2023).

## 6. Conclusions

We have demonstrated that the methodology based on DRCs, incorporating physiological a-priori knowledge pertaining to crop growth, offers substantial benefits compared to statistical models often used in remote sensing, while avoiding the complexity of mechanistic crop growth models. By integrating temperature, an important environmental driver of plant growth, with raw S2 GLAI observations by an probabilistic data assimilation scheme, we were able to reduce the systematic underestimation of high in-situ GLAI values and produce more reliable estimates of crop growth. This approach allowed to preserve the spatial detail of the S2 data, regard physiological constraints on growth predictions and and quantify uncertainties.

We deduce that integrating a-priori physiological understanding by using dose-response curves boasts tremendous potential for promoting agricultural remote sensing generally and crop productivity estimation, specifically. Based on the growing availability of crop phenotyping datasets, this study can serve to enhance both crop growth modelling and agricultural yield estimation.

## Code and Data Availability

Code to reproduce the entire workflow including calibration and validation data is available at `https://github.com/EOA-team/sentinel2_crop_trait_timeseries` under GNU General Public License v3.0.

## Credit Authorship Contribution Statement

Lukas Valentin Graf: Conceptualization, Methodology, Formal analysis, Validation, Visualization, Software, Writing - original draft. Flavian Tschurr: Formal Analysis, Methodology, Software, Methodology, Writing - original draft. Achim Walter: Supervision, Review & Editing. Helge Aasen: Supervision, Review & Editing.

## Declaration of Competing Interest

The authors declare that they have no known competing financial interests or personal relationships that could have appeared to influence the work reported in this paper.

## Acknowledgements

LVG acknowledges funding of the Swiss National Science Foundation for the project “PhenomEn” (grant number IZCOZ0_198091). FT acknowledges funding of the Swiss National Science Foundation for the project "PHENOFLOW" (grant number 200756). The authors thank Stefanie Steinhauser and Tobias Hank, both with the Department of Geography, Ludwig-Maximilians-University Munich, for providing the MNI dataset and for fruitful discussion during the early conceptualisation stage

of our work. Moreover, the authors thank Vilma Rantanen and Karia Kögler (both with ETH Zurich) for their support in the field as well as the field technicians at Agroscope Reckenholz for their support with in-situ sample processing and storage. Furthermore, we thank Marco Landis (Canton of Zurich) for invaluable support at the Strickhof site. At the Swiss Future Farm we thank the team of Michael Simmler (Agroscope Tänikon) and Florian Abt (Canton of Thurgau) for their support and access to the field sites.

## References


Amin, E., Verrelst, J., Rivera-Caicedo, J.P., Pipia, L., Ruiz-Verdú, A., Moreno, J., 2021. Prototyping Sentinel-2 green LAI and brown LAI products for cropland monitoring. Remote Sensing of Environment 255, 112168. URL: https://linkinghub.elsevier.com/retrieve/pii/S0034425720305411, doi:10.1016/j.rse.2020.112168.

Asseng, S., Ewert, F., Martre, P., Rötter, R.P., Lobell, D.B., Cammarano, D., Kimball, B.A., Ottman, M.J., Wall, G.W., White, J.W., Reynolds, M.P., Alderman, P.D., Prasad, P.V.V., Aggarwal, P.K., Anothai, J., Basso, B., Biernath, C., Challinor, A.J., De Sanctis, G., Doltra, J., Fereres, E., Garcia-Vila, M., Gayler, S., Hoogenboom, G., Hunt, L.A., Izaurralde, R.C., Jabloun, M., Jones, C.D., Kersebaum, K.C., Koehler, A.K., Müller, C., Naresh Kumar, S., Nendel, C., O'Leary, G., Olesen, J.E., Palosuo, T., Priesack, E., Eyshi Rezaei, E., Ruane, A.C., Semenov, M.A., Shcherbak, I., Stöckle, C., Stratonovitch, P., Streck, T., Supit, I., Tao, F., Thorburn, P.J., Waha, K., Wang, E., Wallach, D., Wolf, J., Zhao, Z., Zhu, Y., 2015. Rising temperatures reduce global wheat production. Nature Climate Change 5, 143–147. URL: https://www.nature.com/articles/nclimate2470, doi:10.1038/nclimate2470.

Asseng, S., Martre, P., Maiorano, A., Rötter, R.P., O'Leary, G.J., Fitzgerald, G.J., Girousse, C., Motzo, R., Giunta, F., Babar, M.A., Reynolds, M.P., Kheir, A.M.S., Thorburn, P.J., Waha, K., Ruane, A.C., Aggarwal, P.K., Ahmed, M., Balkovič, J., Basso, B., Biernath, C., Bindi, M., Cammarano, D., Challinor, A.J., De Sanctis,

880 G., Dumont, B., Eyshi Rezaei, E., Fereres, E., Ferrise, R., Garcia-Vila, M., Gayler,
881 S., Gao, Y., Horan, H., Hoogenboom, G., Izaurralde, R.C., Jabloun, M., Jones,
882 C.D., Kassie, B.T., Kersebaum, K.C., Klein, C., Koehler, A., Liu, B., Minoli, S.,
883 Montesino San Martin, M., Müller, C., Naresh Kumar, S., Nendel, C., Olesen,
884 J.E., Palosuo, T., Porter, J.R., Priesack, E., Ripoche, D., Semenov, M.A., Stöckle,
885 C., Stratonovitch, P., Streck, T., Supit, I., Tao, F., Van Der Velde, M., Wallach,
886 D., Wang, E., Webber, H., Wolf, J., Xiao, L., Zhang, Z., Zhao, Z., Zhu, Y., Ewert,
887 F., 2019. Climate change impact and adaptation for wheat protein. Global Change
888 Biology 25, 155–173. URL: https://onlinelibrary.wiley.com/doi/10.1111/
889 gcb.14481, doi:10.1111/gcb.14481.

890 Beck, P.S., Atzberger, C., Høgda, K.A., Johansen, B., Skidmore, A.K., 2006.
891 Improved monitoring of vegetation dynamics at very high latitudes: A new
892 method using MODIS NDVI. Remote Sensing of Environment 100, 321–334.
893 URL: https://linkinghub.elsevier.com/retrieve/pii/S0034425705003640,
894 doi:10.1016/j.rse.2005.10.021.

895 Belda, S., Pipia, L., Morcillo-Pallarés, P., Verrelst, J., 2020. Optimizing Gaus-
896 sian Process Regression for Image Time Series Gap-Filling and Crop Monitor-
897 ing. Agronomy 10, 618. URL: https://www.mdpi.com/2073-4395/10/5/618,
898 doi:10.3390/agronomy10050618.

899 Campbell, J.E., Berry, J.A., Seibt, U., Smith, S.J., Montzka, S.A., Launois, T.,
900 Belviso, S., Bopp, L., Laine, M., 2017. Large historical growth in global terrestrial

gross primary production. Nature 544, 84–87. URL: https://www.nature.com/articles/nature22030)., doi:10.1038/nature22030.

Chen, J., Jönsson, P., Tamura, M., Gu, Z., Matsushita, B., Eklundh, L., 2004. A simple method for reconstructing a high-quality NDVI time-series data set based on the Savitzky–Golay filter. Remote Sensing of Environment 91, 332–344. URL: https://linkinghub.elsevier.com/retrieve/pii/S003442570400080X, doi:10.1016/j.rse.2004.03.014.

Cox, G., Gibbons, J., Wood, A., Craigon, J., Ramsden, S., Crout, N., 2006. Towards the systematic simplification of mechanistic models. Ecological Modelling 198, 240–246. URL: https://linkinghub.elsevier.com/retrieve/pii/S0304380006002031, doi:10.1016/j.ecolmodel.2006.04.016.

Danner, M., Berger, K., Wocher, M., Mauser, W., Hank, T., 2017. Retrieval of Biophysical Crop Variables from Multi-Angular Canopy Spectroscopy. Remote Sensing 9, 726. URL: https://www.mdpi.com/2072-4292/9/7/726, doi:10.3390/rs9070726. number: 7 Publisher: Multidisciplinary Digital Publishing Institute.

Danner, M., Berger, K., Wocher, M., Mauser, W., Hank, T., 2019. Fitted PROSAIL Parameterization of Leaf Inclinations, Water Content and Brown Pigment Content for Winter Wheat and Maize Canopies. Remote Sensing 11, 1150. URL: https://www.mdpi.com/2072-4292/11/10/1150, doi:10.3390/rs11101150. number: 10 Publisher: Multidisciplinary Digital Publishing Institute.

Delloye, C., Weiss, M., Defourny, P., 2018. Retrieval of the canopy chlorophyll content from Sentinel-2 spectral bands to estimate nitrogen uptake in

intensive winter wheat cropping systems. Remote Sensing of Environment 216, 245–261. URL: https://www.sciencedirect.com/science/article/pii/S0034425718303158, doi:10.1016/j.rse.2018.06.037.

Delécolle, R., Maas, S.J., Guérif, M., Baret, F., 1992. Remote sensing and crop production models: present trends. ISPRS Journal of Photogrammetry and Remote Sensing 47, 145–161. URL: https://www.sciencedirect.com/science/article/pii/092427169290030D, doi:10.1016/0924-2716(92)90030-D.

Dong, T., Liu, J., Qian, B., Jing, Q., Croft, H., Chen, J., Wang, J., Huffman, T., Shang, J., Chen, P., 2017. Deriving Maximum Light Use Efficiency From Crop Growth Model and Satellite Data to Improve Crop Biomass Estimation. IEEE Journal of Selected Topics in Applied Earth Observations and Remote Sensing 10, 104–117. URL: https://ieeexplore.ieee.org/abstract/document/7592477, doi:10.1109/JSTARS.2016.2605303.

Eilers, P.H.C., 2003. A Perfect Smoother. Analytical Chemistry 75, 3631–3636. URL: https://pubs.acs.org/doi/10.1021/ac034173t, doi:10.1021/ac034173t.

Evensen, G., 2003. The Ensemble Kalman Filter: theoretical formulation and practical implementation. Ocean Dynamics 53, 343–367. URL: http://link.springer.com/10.1007/s10236-003-0036-9, doi:10.1007/s10236-003-0036-9.

Féret, J.B., Gitelson, A., Noble, S., Jacquemoud, S., 2017. PROSPECT-D: Towards modeling leaf optical properties through a complete lifecycle. Remote Sensing of Environment 193, 204–215. URL: https://linkinghub.elsevier.com/retrieve/pii/S0034425717300962, doi:10.1016/j.rse.2017.03.004.

945 Gitelson, A.A., Peng, Y., Arkebauer, T.J., Suyker, A.E., 2015. Productivity, ab-
946 sorbed photosynthetically active radiation, and light use efficiency in crops: Impli-
947 cations for remote sensing of crop primary production. Journal of Plant Physiology
948 177, 100–109. URL: https://www.sciencedirect.com/science/article/pii/
949 S0176161715000073, doi:10.1016/j.jplph.2014.12.015.

950 Graf, L.V., Gorroño, J., Hueni, A., Walter, A., Aasen, H., 2023a. Propagating
951 sentinel-2 top-of-atmosphere radiometric uncertainty into land surface phenology
952 metrics using a monte carlo framework. IEEE Journal of Selected Topics in Ap-
953 plied Earth Observations and Remote Sensing , 1–41doi:10.1109/JSTARS.2023.
954 3297713.

955 Graf, L.V., Merz, Q.N., Walter, A., Aasen, H., 2023b. Insights from field phe-
956 notyping improve satellite remote sensing based in-season estimation of winter
957 wheat growth and phenology. Remote Sensing of Environment 299, 113860.
958 URL: https://linkinghub.elsevier.com/retrieve/pii/S003442572300411X,
959 doi:10.1016/j.rse.2023.113860.

960 Graf, L.V., Perich, G., Aasen, H., 2022. EOdal: An open-source Python
961 package for large-scale agroecological research using Earth Observation and
962 gridded environmental data. Computers and Electronics in Agriculture
963 203, 107487. URL: https://www.sciencedirect.com/science/article/pii/
964 S0168169922007955, doi:10.1016/j.compag.2022.107487.

965 Hank, T.B., Bach, H., Mauser, W., 2015. Using a Remote Sensing-Supported
966 Hydro-Agroecological Model for Field-Scale Simulation of Heterogeneous Crop

967 Growth and Yield: Application for Wheat in Central Europe. Remote Sensing 7,
968 3934–3965. URL: https://www.mdpi.com/2072-4292/7/4/3934, doi:10.3390/
969 rs70403934. number: 4 Publisher: Multidisciplinary Digital Publishing Institute.

970 Hilty, J., Muller, B., Pantin, F., Leuzinger, S., 2021. Plant growth: the What,
971 the How, and the Why. New Phytologist 232, 25–41. URL: https://nph.
972 onlinelibrary.wiley.com/doi/10.1111/nph.17610, doi:10.1111/nph.17610.

973 Huang, J., Gómez-Dans, J.L., Huang, H., Ma, H., Wu, Q., Lewis, P.E., Liang,
974 S., Chen, Z., Xue, J.H., Wu, Y., Zhao, F., Wang, J., Xie, X., 2019. Assimi-
975 lation of remote sensing into crop growth models: Current status and perspec-
976 tives. Agricultural and Forest Meteorology 276-277, 107609. URL: https://www.
977 sciencedirect.com/science/article/pii/S0168192319302175, doi:10.1016/
978 j.agrformet.2019.06.008.

979 Huang, J., Sedano, F., Huang, Y., Ma, H., Li, X., Liang, S., Tian, L., Zhang, X.,
980 Fan, J., Wu, W., 2016. Assimilating a synthetic Kalman filter leaf area index
981 series into the WOFOST model to improve regional winter wheat yield estima-
982 tion. Agricultural and Forest Meteorology 216, 188–202. URL: https://www.
983 sciencedirect.com/science/article/pii/S0168192315007480, doi:10.1016/
984 j.agrformet.2015.10.013.

985 Jacquemoud, S., Verhoef, W., Baret, F., Bacour, C., Zarco-Tejada, P.J., As-
986 ner, G.P., François, C., Ustin, S.L., 2009. PROSPECT+SAIL models: A re-
987 view of use for vegetation characterization. Remote Sensing of Environment

113, S56–S66. URL: https://www.sciencedirect.com/science/article/pii/S0034425709000765, doi:10.1016/j.rse.2008.01.026.

Jamieson, P.D., Semenov, M.A., Brooking, I.R., Francis, G.S., 1998. Sirius: A mechanistic model of wheat response to environmental variation. European Journal of Agronomy 8, 161–179. doi:10.1016/S1161-0301(98)00020-3.

Johnson, S.G., 2007. The NLopt nonlinear-optimization package. https://github.com/stevengj/nlopt.

Keating, B.A., Carberry, P.S., Hammer, G.L., Probert, M.E., Robertson, M.J., Holzworth, D., Huth, N.I., Hargreaves, J.N.G., Meinke, H., Hochmann, Z., McLean, G., Verburg, K., Snow, V., Dimes, J., Silburn, M., Wang, E., Brown, S., Bristow, K., Asseng, S., Chapman, S., McCown, R., Freebairn, D., Smith, C., 2003. An overview of APSIM, a model designed for farming systems simulation. European Journal of Agronomy 18, 267–288. doi:https://doi.org/10.1016/S1161-0301(02)00108-9.

Koetz, B., Baret, F., Poilvé, H., Hill, J., 2005. Use of coupled canopy structure dynamic and radiative transfer models to estimate biophysical canopy characteristics. Remote Sensing of Environment 95, 115–124. URL: https://www.sciencedirect.com/science/article/pii/S0034425704003736, doi:10.1016/j.rse.2004.11.017.

Kooistra, L., Berger, K., Brede, B., Graf, L.V., Aasen, H., Roujean, J.L., Machwitz, M., Schlerf, M., Atzberger, C., Prikaziuk, E., Ganeva, D., Tomelleri,

E., Croft, H., Reyes Muñoz, P., Garcia Millan, V., Darvishzadeh, R., Koren, G., Herrmann, I., Rozenstein, O., Belda, S., Rautiainen, M., Rune Karlsen, S., Figueira Silva, C., Cerasoli, S., Pierre, J., Tanır Kayıkçı, E., Halabuk, A., Tunc Gormus, E., Fluit, F., Cai, Z., Kycko, M., Udelhoven, T., Verrelst, J., 2023. Reviews and syntheses: Remotely sensed optical time series for monitoring vegetation productivity. Biogeosciences Discussions , 1–67URL: https://bg.copernicus.org/preprints/bg-2023-88/, doi:10.5194/bg-2023-88.

Kronenberg, L., Yu, K., Walter, A., Hund, A., 2017. Monitoring the dynamics of wheat stem elongation : genotypes differ at critical stages. Euphytica 213, 1:13. doi:10.1007/s10681-017-1940-2.

Lancashire, P.D., Bleiholder, H., Boom, T.V.D., Langelüddeke, P., Stauss, R., Weber, E., Witzenberger, A., 1991. A uniform decimal code for growth stages of crops and weeds. Annals of Applied Biology 119, 561–601. URL: https://onlinelibrary.wiley.com/doi/abs/10.1111/j.1744-7348.1991.tb04895.x, doi:10.1111/j.1744-7348.1991.tb04895.x. _eprint: https://onlinelibrary.wiley.com/doi/pdf/10.1111/j.1744-7348.1991.tb04895.x.

Ma, C., Liu, M., Ding, F., Li, C., Cui, Y., Chen, W., Wang, Y., 2022. Wheat growth monitoring and yield estimation based on remote sensing data assimilation into the SAFY crop growth model. Scientific Reports 12, 5473. URL: https://www.nature.com/articles/s41598-022-09535-9, doi:10.1038/s41598-022-09535-9.

Maddonni, G.A., Otegui, M.E., 1996. Leaf area, light interception, and crop

development in maize. Field Crops Research 48, 81–87. URL: https://www.sciencedirect.com/science/article/pii/0378429096000354, doi:10.1016/0378-4290(96)00035-4.

Mcmaster, G., 1997. Growing degree-days: one equation, two interpretations. Agricultural and Forest Meteorology 87, 291–300. URL: https://linkinghub.elsevier.com/retrieve/pii/S0168192397000270, doi:10.1016/S0168-1923(97)00027-0.

Meenken, E.D., Triggs, C.M., Brown, H.E., Sinton, S., Bryant, J.R., Noble, A.D., Espig, M., Sharifi, M., Wheeler, D.M., 2021. Bayesian hybrid analytics for uncertainty analysis and real-time crop management. Agronomy Journal 113, 2491–2505. URL: https://onlinelibrary.wiley.com/doi/10.1002/agj2.20659, doi:10.1002/agj2.20659.

Miralles, D.J., Richards, R.A., Slafer, G.A., 2000. Duration of the stem elongation period influences the number of fertile florets in wheat and barley. Functional Plant Biology 27, 931–940. URL: https://www.publish.csiro.au/fp/pp00021, doi:10.1071/PP00021.

Monsi, M., Seaki, T., 2004. On the Factor Light in Plant Communities and its Importance for Matter Production. Annals of Botany 95, 549–567. URL: https://academic.oup.com/aob/article-lookup/doi/10.1093/aob/mci052, doi:10.1093/aob/mci052.

Parent, B., Tardieu, F., 2012. Temperature responses of developmental processes have not been affected by breeding in different ecological areas for 17 crop species.

New Phytologist 194, 760–774. URL: https://onlinelibrary.wiley.com/doi/10.1111/j.1469-8137.2012.04086.x, doi:10.1111/j.1469-8137.2012.04086.x.

Pask, A., Pietragalla, J., Mullan, D., Reynolds, M.P., 2012. Physiological breeding II: a field guide to wheat phenotyping URL: https://repository.cimmyt.org/handle/10883/1288. accepted: 2012-02-24T23:09:09Z Publisher: CIMMYT.

Pellenq, J., Boulet, G., 2004. A methodology to test the pertinence of remote-sensing data assimilation into vegetation models for water and energy exchange at the land surface. Agronomie 24, 197–204. URL: http://www.edpsciences.org/10.1051/agro:2004017, doi:10.1051/agro:2004017.

Pipia, L., Amin, E., Belda, S., Salinero-Delgado, M., Verrelst, J., 2021. Green LAI Mapping and Cloud Gap-Filling Using Gaussian Process Regression in Google Earth Engine. Remote Sensing 13, 403. URL: https://www.mdpi.com/2072-4292/13/3/403, doi:10.3390/rs13030403.

Porter, J.R., Gawith, M., 1999. Temperatures and the growth and development of wheat: a review. European Journal of Agronomy 10, 23–36. URL: https://www.sciencedirect.com/science/article/pii/S1161030198000471, doi:10.1016/S1161-0301(98)00047-1.

Powell, M.J.D., 1994. A direct search optimization method that models the objective and constraint functions by linear interpolation, in: Gomez, S., Hennart, J.P. (Eds.), Advances in Optimization and Numerical Analysis. Springer.

volume 275 of *Mathematics and Its Applications*, pp. 51–67. doi:10.1007/978-94-015-8330-5{_}4.

R Core Team, 2018. R: A Language and Environment for Statistical Computing. R Foundation for Statistical Computing, Vienna. .

Reichenau, T.G., Korres, W., Schmidt, M., Graf, A., Welp, G., Meyer, N., Stadler, A., Brogi, C., Schneider, K., 2020. A comprehensive dataset of vegetation states, fluxes of matter and energy, weather, agricultural management, and soil properties from intensively monitored crop sites in western Germany. Earth System Science Data 12, 2333–2364. URL: https://essd.copernicus.org/articles/12/2333/2020/, doi:10.5194/essd-12-2333-2020.

Reynolds, M., Langridge, P., 2016. Physiological breeding. Current Opinion in Plant Biology 31, 162–171. doi:10.1016/j.pbi.2016.04.005.

Richter, K., Atzberger, C., Vuolo, F., D'Urso, G., 2011. Evaluation of Sentinel-2 Spectral Sampling for Radiative Transfer Model Based LAI Estimation of Wheat, Sugar Beet, and Maize. IEEE Journal of Selected Topics in Applied Earth Observations and Remote Sensing 4, 458–464. doi:10.1109/JSTARS.2010.2091492.

Roth, L., Binder, M., Kirchgessner, N., Tschurr, F., Yates, S., Hund, A., Kronenberg, L., Walter, A., 2023. Field phenotyping reveals the importance of including cultivar-specific per se temperature response in phenology modeling. URL: https://www.biorxiv.org/content/10.1101/2023.08.29.555271v1, doi:10.1101/2023.08.29.555271.

Roth, L., Piepho, H.P., Hund, A., 2022. Phenomics data processing: extracting dose–response curve parameters from high-resolution temperature courses and repeated field-based wheat height measurements. in silico Plants 4, diac007. URL: https://doi.org/10.1093/insilicoplants/diac007, doi:10.1093/insilicoplants/diac007.

Sadeh, Y., Zhu, X., Dunkerley, D., Walker, J.P., Zhang, Y., Rozenstein, O., Manivasagam, V., Chenu, K., 2021. Fusion of Sentinel-2 and PlanetScope time-series data into daily 3 m surface reflectance and wheat LAI monitoring. International Journal of Applied Earth Observation and Geoinformation 96, 102260. URL: https://linkinghub.elsevier.com/retrieve/pii/S030324342030903X, doi:10.1016/j.jag.2020.102260.

Savitzky, A., Golay, M.J.E., 1964. Smoothing and Differentiation of Data by Simplified Least Squares Procedures. Analytical Chemistry 36, 1627–1639. URL: https://pubs.acs.org/doi/abs/10.1021/ac60214a047, doi:10.1021/ac60214a047.

Sudmanns, M., Tiede, D., Augustin, H., Lang, S., 2020. Assessing global Sentinel-2 coverage dynamics and data availability for operational Earth observation (EO) applications using the EO-Compass. International Journal of Digital Earth 13, 768–784. URL: https://www.tandfonline.com/doi/full/10.1080/17538947.2019.1572799, doi:10.1080/17538947.2019.1572799.

Tilman, D., Balzer, C., Hill, J., Befort, B.L., 2011. Global food demand and the sustainable intensification of agriculture. Proceedings of the National Academy of

1116 Sciences of the United States of America 108, 20260–20264. doi:10.1073/pnas.
1117 1116437108.

1118 Tschurr, F., Feigenwinter, I., Fischer, A.M., Kotlarski, S., 2020. Climate scenarios
1119 and agricultural indices: A case study for Switzerland. Atmosphere 11, 1–23.
1120 doi:10.3390/atmos11050535.

1121 Tschurr, F., Kirchgessner, N., Hund, A., Kronenberg, L., Anderegg, J., Walter,
1122 A., Roth, L., 2023. Frost Damage Index: The Antipode of Growing Degree
1123 Days. Plant Phenomics 5, 0104. URL: https://spj.science.org/doi/10.
1124 34133/plantphenomics.0104, doi:10.34133/plantphenomics.0104.

1125 Verhoef, W., 1984. Light scattering by leaf layers with application to canopy
1126 reflectance modeling: The SAIL model. Remote Sensing of Environment
1127 16, 125–141. URL: https://www.sciencedirect.com/science/article/pii/
1128 0034425784900579, doi:10.1016/0034-4257(84)90057-9.

1129 Waldner, F., Horan, H., Chen, Y., Hochman, Z., 2019. High temporal resolution of
1130 leaf area data improves empirical estimation of grain yield. Scientific Reports
1131 9, 15714. URL: https://www.nature.com/articles/s41598-019-51715-7,
1132 doi:10.1038/s41598-019-51715-7.

1133 Wang, E., Engel, T., 1998. Simulation of Phenological Development of Wheat Crops.
1134 Agricultural Systems 58, 1–24. doi:https://doi.org/10.1016/S0308-521X(98)
1135 00028-6.

1136 Wang, E., Martre, P., Zhao, Z., Ewert, F., Maiorano, A., Rötter, R.P., Kimball,

B.A., Ottman, M.J., Wall, G.W., White, J.W., Reynolds, M.P., Alderman, P.D., Aggarwal, P.K., Anothai, J., Basso, B., Biernath, C., Cammarano, D., Challinor, A.J., De Sanctis, G., Doltra, J., Fereres, E., Garcia-Vila, M., Gayler, S., Hoogenboom, G., Hunt, L.A., Izaurralde, R.C., Jabloun, M., Jones, C.D., Kersebaum, K.C., Koehler, A.K., Liu, L., Müller, C., Naresh Kumar, S., Nendel, C., O'Leary, G., Olesen, J.E., Palosuo, T., Priesack, E., Eyshi Rezaei, E., Ripoche, D., Ruane, A.C., Semenov, M.A., Shcherbak, I., Stöckle, C., Stratonovitch, P., Streck, T., Supit, I., Tao, F., Thorburn, P., Waha, K., Wallach, D., Wang, Z., Wolf, J., Zhu, Y., Asseng, S., 2017. The uncertainty of crop yield projections is reduced by improved temperature response functions. Nature Plants 2017 3:8 3, 1–13. URL: https://www.nature.com/articles/nplants2017102, doi:10.1038/nplants.2017.102.

Weiss, M., Jacob, F., Duveiller, G., 2020. Remote sensing for agricultural applications: A meta-review. Remote Sensing of Environment 236, 111402. URL: https://www.sciencedirect.com/science/article/pii/S0034425719304213, doi:10.1016/j.rse.2019.111402.

Wildhaber, S., Graf, L.V., Aasen, H., 2023. Assessing the Potential of HighResolution Satellite Constellations for Agricultural Monitoring, Munich.

de Wit, A.J.W., van Diepen, C.A., 2007. Crop model data assimilation with the Ensemble Kalman filter for improving regional crop yield forecasts. Agricultural and Forest Meteorology 146, 38–56. URL: https://www.

1158 sciencedirect.com/science/article/pii/S0168192307001402, doi:10.1016/
1159 j.agrformet.2007.05.004.

1160 Wocher, M., Berger, K., Danner, M., Mauser, W., Hank, T., 2018. Physically-Based
1161 Retrieval of Canopy Equivalent Water Thickness Using Hyperspectral Data. Re-
1162 mote Sensing 10, 1924. URL: https://www.mdpi.com/2072-4292/10/12/1924,
1163 doi:10.3390/rs10121924. number: 12 Publisher: Multidisciplinary Digital Pub-
1164 lishing Institute.

1165 Wocher, M., Berger, K., Danner, M., Mauser, W., Hank, T., 2020. RTM-based
1166 dynamic absorption integrals for the retrieval of biochemical vegetation traits. In-
1167 ternational Journal of Applied Earth Observation and Geoinformation 93, 102219.
1168 URL: https://linkinghub.elsevier.com/retrieve/pii/S0303243420305754,
1169 doi:10.1016/j.jag.2020.102219.

1170 Zeng, L., Wardlow, B.D., Xiang, D., Hu, S., Li, D., 2020. A review of vegetation phe-
1171 nological metrics extraction using time-series, multispectral satellite data. Remote
1172 Sensing of Environment 237, 111511. URL: https://www.sciencedirect.com/
1173 science/article/pii/S0034425719305309, doi:10.1016/j.rse.2019.111511.

1174 Zhang, C., Liu, J., Shang, J., Dong, T., Tang, M., Feng, S., Cai, H., 2021. Improv-
1175 ing winter wheat biomass and evapotranspiration simulation by assimilating leaf
1176 area index from spectral information into a crop growth model. Agricultural Wa-
1177 ter Management 255, 107057. URL: https://www.sciencedirect.com/science/
1178 article/pii/S037837742100322X, doi:10.1016/j.agwat.2021.107057.

Zhao, Y., Chen, S., Shen, S., 2013. Assimilating remote sensing information with crop model using Ensemble Kalman Filter for improving LAI monitoring and yield estimation. Ecological Modelling 270, 30–42. URL: https://www.sciencedirect.com/science/article/pii/S030438001300416X, doi:10.1016/j.ecolmodel.2013.08.016.

Zhou, J., Jia, L., Menenti, M., 2015. Reconstruction of global MODIS NDVI time series: Performance of Harmonic ANalysis of Time Series (HANTS). Remote Sensing of Environment 163, 217–228. URL: https://linkinghub.elsevier.com/retrieve/pii/S0034425715001145, doi:10.1016/j.rse.2015.03.018.

Zhou, J., Jia, L., Menenti, M., Gorte, B., 2016. On the performance of remote sensing time series reconstruction methods – A spatial comparison. Remote Sensing of Environment 187, 367–384. URL: https://www.sciencedirect.com/science/article/pii/S0034425716303972, doi:10.1016/j.rse.2016.10.025.

## Appendix A. Supplementary Materials

Table A.6: Overview of the spectral bands of the multispectral-imager instrument onboard the S2A and S2B satellites provided by the European Space Agency, ESA (`https://sentinels.copernicus.eu/web/sentinel/technical-guides/sentinel-2-msi/msi-instrument`). Band widths and wavelengths are provided in nm, the spatial resolution in m.

| **S2A** | | | **S2B** | | |
|---|---|---|---|---|---|
| **Band** | **Central wavelength** | **Bandwidth** | **Central wavelength** | **Bandwidth** | **Spatial resolution** |
| 1 | 442.7 | 20 | 442.3 | 20 | 60 |
| 2 | 492.7 | 65 | 492.3 | 65 | 10 |
| 3 | 559.8 | 35 | 558.9 | 35 | 10 |
| 4 | 664.6 | 30 | 664.9 | 31 | 10 |
| 5 | 704.1 | 14 | 703.8 | 15 | 20 |
| 6 | 740.5 | 14 | 739.1 | 13 | 20 |
| 7 | 782.8 | 19 | 779.7 | 19 | 20 |
| 8 | 832.8 | 105 | 832.9 | 104 | 10 |
| 8a | 864.7 | 21 | 864.0 | 21 | 20 |
| 9 | 945.1 | 19 | 943.2 | 20 | 60 |
| 10 | 1373.5 | 29 | 1376.9 | 29 | 60 |
| 11 | 1613.7 | 90 | 1610.4 | 94 | 20 |
| 12 | 2202.4 | 174 | 2185.7 | 184 | 20 |

Table A.7: Overview of the start parameter, lower and upper boundaries for the parameter estimation. For environment dependent parameters, the corresponding quantiles (Q) have been considered. For the environment independent parameters prior knowledge was used to determine the start values.

| dose response curve | parameter name | lower | start | upper |
|---|---|---|---|---|
| non linear | $T_{base}$ | Q 0.05 | Q 0.1 | Q 0.6 |
| non linear | slope | 0 | 0.05 | 0.5 |
| asymptotic | $T_{base}$ | Q 0.01 | Q 0.1 | Q 0.4 |
| asymptotic | lrc | -15 | -1 | 1.5 |
| asymptotic | asymptote | Q 0.6 | Q 0.9 | Q 0.98 |
| Wang Engels | $T_{base}$ | Q 0.1 | Q 0.25 | Q 0.4 |
| Wang Engels | $T_{opt}$ | Q 0.6 | Q 0.85 | Q 0.98 |
| Wang Engels | $T_{max}$ | Q 0.7 | Q 0.95 | Q 0.99 |